

# New Calculations of Stark Broadened Profiles for Neutral Helium Lines Using Computer Simulations

Patrick Tremblay, A. Beauchamp, and P. Bergeron

*Département de Physique, Université de Montréal, C.P. 6128, Succ. Centre-Ville,  
Montréal, Québec H3C 3J7, Canada*

patrick@astro.umontreal.ca, bergeron@astro.umontreal.ca

## ABSTRACT

We present new calculations of Stark broadened profiles for neutral helium lines using computer simulations that include some important aspects aimed at better representing the dynamical environment of the helium atom. These include the unification of ion and electron treatment, the correction for ion dynamics, the transition of the electron contribution to broadening from the core to the wings of the profile, the numerical integration of the time evolution operator of helium perturbed by a fluctuating electric field, the Debye correction for the correlation of the motion of charged perturbers, local density variations, and particle reinjection. We compare the results of our simulations for the He I  $\lambda\lambda 4471$  and  $4922$  lines with other results published in the literature. We also test our simulation environment for narrow lines (He I  $\lambda\lambda 5877$  and  $6678$ ) and broader lines (He I  $\lambda\lambda 4026$  and  $4144$ ). We find that the narrow lines are more difficult to produce adequately than the the broader ones.

## 1. Introduction

For nearly three decades, the atmospheric parameters of white dwarf stars have been measured using the so-called spectroscopic technique, where absorption line profiles are fitted with the predictions of detailed model atmospheres (see, e.g, Bergeron et al. 1992; Eisenstein et al. 2006; Kepler et al. 2007; Tremblay et al. 2011; Koester & Kepler 2015; Genest-Beaulieu & Bergeron 2019a). In this case the effective temperature ( $T_{\text{eff}}$ ), surface gravity ( $\log g$ ), and the chemical abundances can be measured, while the other stellar parameters such as the stellar mass and radius, cooling age, etc., can be derived from evolutionary models. Thanks to the Sloan Digital Sky Survey (SDSS), atmospheric and physical parameters have now been determined for tens of thousand white dwarfs (see, e.g., Kepler et al. 2019). While the

spectroscopic technique is arguably the most accurate approach to measure white dwarf parameters because of the physical information contained in the line profiles, it is also strongly dependent on the validity of the line profile calculations (see Tremblay & Bergeron 2009 for the case of Stark broadening of hydrogen lines). Also, the spectroscopic technique can only be applied to white dwarfs that are hot enough to show strong absorption lines, which corresponds roughly to  $T_{\text{eff}} > 6500$  K for DA stars, and  $T_{\text{eff}} > 13,000$  K for DB stars. Thus white dwarfs close to the peak of the white dwarf luminosity function cannot be studied using this method.

An alternative approach that can be applied to any type of white dwarf with relative accuracy is the photometric technique (Bergeron et al. 1997), where the overall spectral energy distribution built from observed magnitudes (converted into average fluxes) are fitted with synthetic photometry obtained from model spectra. In this case, the effective temperature and the solid angle —  $\pi(R/D)^2$  where  $R$  is the stellar radius and  $D$  the distance from Earth — are considered free parameters, which implies that in order to measure the radius (and other stellar parameters such as the mass), the distance to each object must be known from trigonometric parallax measurements. The photometric technique has been applied by Bergeron et al. (2001) to nearly all white dwarfs with trigonometric parallaxes available at that time, which unfortunately, included only a few hundred objects. Also, the optical *BVRI* and infrared *JHK* photometry they used was painstakingly secured object by object. Now thanks to the recent astrometric *Gaia* mission (Gaia Collaboration et al. 2018), precise astrometric and photometric data for  $\sim 260,000$  high-confidence white dwarf candidates have now become available. Furthermore, large (almost) all-sky surveys are now providing exquisite photometric data, for instance *ugriz* photometry from SDSS, or *grizy* photometry from Pan-STARRS (Panoramic Survey Telescope And Rapid Response System; Tonry et al. 2012).

Recently, Genest-Beaulieu & Bergeron (2019a, see also Genest-Beaulieu & Bergeron 2019b for a more thorough analysis of DB stars) presented a detailed spectroscopic and photometric analysis of DA and DB white dwarfs drawn from the SDSS with trigonometric parallax measurements available from the *Gaia* mission. While in principle both sets of parameters obtained from spectroscopy and photometry should agree, large discrepancies have been identified in terms of effective temperature and mass determinations (or equivalently,  $\log g$ ). Although uncertainties in the treatment of line broadening theory, convective energy transport, and perhaps chemical composition have been invoked to account for these discrepancies, it is also possible that calibration problems with the photometric and/or spectroscopic data play an important role (Bergeron et al. 2019). In order to understand better the nature of these discrepancies, every specific ingredient of both the spectroscopic and photometric techniques needs to be scrutinized in detail, both theoretically and observationally.

In this paper, we focus our attention on the Stark broadening of neutral helium lines used in model atmosphere calculations of DB/DO white dwarfs.

The main line broadening mechanism in hot ( $T_{\text{eff}} \gtrsim 15,000$  K) DB white dwarfs is Stark broadening, which is caused by the presence of charged perturbers in the surrounding plasma. Historically, the neutral helium lines were treated within the semi-classical theory of overlapping lines introduced by Baranger (1958a,b), which consists of considering classical perturbers around a helium atom described by quantum mechanics. A few detailed line profile calculations became available where the quasi-static approximation was used for the ions, together with the impact approximation for the electrons; in these calculations, the influence of neighboring energy levels to the observed transition was considered, giving rise to the so-called forbidden components. These calculations include He I  $\lambda 4471$  (Gieske & Griem 1969; Barnard et al. 1969), He I  $\lambda 4922$  (Barnard et al. 1969), He I  $\lambda 5016$  (Barnard & Cooper 1970), He I  $\lambda 4388$  (Shamey 1969), He I  $\lambda 4026$  (Shamey 1969; Gieske & Griem 1969), and He I  $\lambda 6678$  (Ya’akobi et al. 1972). Barnard et al. (1974) and Barnard et al. (1975) then computed a new series of line profiles for  $\lambda 4471$  and  $\lambda 4922$ , respectively, by including the one-electron approximation from Baranger (1962), which provides a better transition between the impact approximation and the quasi-static contribution of the electrons, along with ion dynamics corrections. Unfortunately, the other helium lines in the optical were still calculated using the isolated line approximation of the theory, thus neglecting the contributions of the forbidden components to the line profile (used by Griem 1974 and Dimitrijevic & Sahal-Brechot 1984). The limited access to detailed neutral helium line profiles in the optical proved to be a major obstacle to perform reliable spectroscopic analyses of DB white dwarfs.

To remedy this situation, Beauchamp et al. (1997, see also Beauchamp 1995) produced detailed line profile calculations for most neutral helium lines in the optical using the same semi-classical approximation as described above, by also including the one-electron approximation while the ions were still considered within the quasi-static approximation. These detailed line profiles significantly improved the spectroscopic analyses of DB white dwarfs (Beauchamp et al. 1996, Voss et al. 2007, Bergeron et al. 2011, Koester & Kepler 2015, Genest-Beaulieu & Bergeron 2019b), and they remain the ultimate reference in the field as of today. However, the downside of the semi-analytical approach used by Beauchamp et al. is the theoretical limitations describing the analytical contribution to the line profile from both the ions and the electrons. Even if there are several approximations for the electrons — namely the impact and one-electron approximations — for different regimes of interest, the smooth transition between these two is not guaranteed. Also, the quasi-static approximation becomes problematic in the line cores where ion dynamics contribute, in particular at lower electron densities (Barnard et al. 1974, 1975; Gigosos & Cardeñoso 1996; Omar et al. 2006; Ben Chaouacha et al. 2007; Gigosos 2014).

An alternative approach to the semi-analytical calculations performed by Beauchamp et al. (1997) is to produce full-fledged computer simulations. This approach has first been introduced by Stamm & Voslamber (1979) to study the effect of ion dynamics on the Ly $\beta$  hydrogen line. The method consists in generating a time sequence of electric fields to represent their statistical distributions in a natural way using a simple plasma model formed by charged particles (perturbers) and emitters (neutral or charged). Although the method appeared like an ideal experiment, computational time was the largest obstacle, as well as the crude treatment of the limited simulated volume. It is not until Gigosos et al. (1985) that the computing time was reduced using an improved differential equation solving algorithm for the evolution of the emitter for hydrogen. This allowed the calculations of spectra of hydrogen Balmer lines, and Stark broadening could now be considered in more detail using a new particle re-injection technique (Gigosos & Cardenoso 1987; Gigosos & Cardenoso 1996), in combination with a more adequate spherical simulation volume, instead of a cubic volume. It was also demonstrated that one could remove the limitations of a finite simulation volume (Hegerfeldt & Kesting 1988). Improvements to these techniques in the following years (Calisti et al. 1988; Frerichs 1989; Poquérusse et al. 1996; Halenka & Olchawa 1996; Alexiou et al. 1999a,b; Sorge & Günter 2000; Olchawa 2002; Wujec et al. 2002; Halenka et al. 2002; Wujec et al. 2003; Olchawa et al. 2004; Stambulchik & Maron 2006; Stambulchik et al. 2007; Gigosos et al. 2018) allowed the calculations of both hydrogen (Gigosos & Cardenoso 1996; Gigosos et al. 2003; Gomez 2017) and neutral helium (Gigosos & González 2009; Lara et al. 2012) Stark broadened line profiles. The simulation method is now gaining more and more attention (Gigosos 2014), even though the computational time remains the largest obstacle as we gradually converge towards a more physically representative simulation (Gigosos et al. 2018).

We report in this paper the results of our own computer simulations, performed by combining the method developed by Gigosos & Cardenoso (1996) for treating naturally the dynamics of the environment around the emitting neutral helium atom, and the approach of Hegerfeldt & Kesting (1988) for dealing with local density variations. The theoretical background and the standard Stark broadening theory are first described in Sections 2 and 3, respectively. We then discuss in Section 4 the details of our computer simulations, including the generation and reinjection of particles in the simulation volume, and the time evolution operator. We finally present in Section 5 our results for the He I  $\lambda\lambda$ 4026, 4144, 4471, 4922, 5877, and 6678 lines, and compare our line profiles with those published by Beauchamp et al. (1997), Gigosos & González (2009), and Lara et al. (2012); comparisons of synthetic spectra of DB white dwarfs for He I  $\lambda$ 4471 and  $\lambda$ 4922 are also discussed. Our conclusions follow in Section 6.

## 2. Theoretical Background

### 2.1. Fundamental Aspects of the Stark Broadening Theory

Most Stark-broadened line profile calculations for He I lines are based on the semi-classical theory of Stark broadening of Baranger (1958b, see also Baranger 1962; Sahal-Brechot 1969a; Smith et al. 1969; Griem 1974; Gigosos 2014). The charged particles, electrons and ions, which perturb the emitting helium atom move along classical paths that are independent of the state of the atom, while the spectral distribution of the light emitted by the atom is computed quantum-mechanically. Since the model is developed within the coordinate system of the emitter, the effects induced by the motion of the emitters relative to the observer are not taken into account, and the computed Stark profile must thus subsequently be convoluted with a Gaussian Doppler profile.

The development of the Stark broadening theory starts with an isolated quantum system in thermodynamic equilibrium, composed of a single emitter at rest interacting with charged perturbers with no internal structure. The type and number density of the perturbers are consistent with the given macroscopic properties of the gas (temperature, electron number density, and chemical composition). The Hamiltonian of the system can be written as

$$H = H_0 + H_p + V \quad (1)$$

where  $H_0$  is the Hamiltonian of the isolated emitter,  $H_p$  is the Hamiltonian of the perturbers, including their mutual interactions, and  $V$  is the interaction between the neutral emitter and the perturbers. Since the system is in thermodynamic equilibrium, the Hamiltonian has no explicit time dependence, which implies that its eigenstates have well-defined energies.

The power spectrum  $P(\omega)$  of the plasma is defined as the power emitted per unit frequency interval. The expression for the spontaneous emission rate of an isolated atom can be generalized for the whole quantum system as a weighted sum over all possible spontaneous transitions  $|i\rangle \rightarrow |f\rangle$  between initial and final eigenstates of the Hamiltonian (Equation 1),

$$P(\omega) = \frac{4\pi\omega^4}{3c^3} \sum_{if} \delta(\omega - \omega_{if}) |\langle f | \mathbf{d} | i \rangle|^2 \rho_i, \quad (2)$$

where  $\omega_{if} = (E_i - E_f)/\hbar$  is the angular frequency of the emitted photon,  $\mathbf{d}$  is the electric dipole moment operator of the whole system, and  $\rho_i$  is the statistical weight of the initial state of the transition, i.e., its Boltzmann factor given by

$$\rho_i \propto e^{-E_i/kT} , \quad (3)$$

whose sum over all initial states is normalized to unit area.

Since we only calculate the spectrum of the emitter, the contribution of the perturbbers to the dipole moment is generally omitted. In the particular case where the emitter is a helium atom, all the lines in the optical region of the spectrum are the result of transitions between singly excited states, that is, with one electron staying in the ground state. The dipole moment then reduces to that of the single electron in the excited state,

$$\mathbf{d} = e\mathbf{R} , \quad (4)$$

where  $e$  is the elementary charge, and  $\mathbf{R}$  the position operator of the electron.

One generally discards the physical constants and the slowly varying  $\omega^4$  term in Equation (2), and redefines the profile as

$$I(\omega) = \sum_{if} \delta(\omega - \omega_{if}) |\langle f | \mathbf{d} | i \rangle|^2 \rho_i . \quad (5)$$

In practice, it is usually easier to work in the time domain, and to compute directly the Fourier transform of the profile, called the autocorrelation function

$$C(t) = \int_{-\infty}^{+\infty} dt e^{-i\omega t} I(\omega) = \sum_{if} e^{-i\omega_{if}t} |\langle f | \mathbf{d} | i \rangle|^2 \rho_i , \quad (6)$$

where  $C(t)$  satisfies the condition  $C(-t) = C^*(t)$  since  $I(\omega)$  is real. The profile can then be recovered by performing the inverse Fourier transform

$$I(\omega) = \frac{1}{\pi} \text{Re} \int_0^{\infty} dt e^{i\omega t} C(t) , \quad (7)$$

where the above condition on  $C(t)$  is explicitly taken into account. The theoretical development now focuses on the detailed calculations of  $C(t)$  from the dynamics of the system.

Equation (6) is tied to a particular basis, the energy eigenstates of the whole system. It is thus advantageous to express  $C(t)$  with quantum operators only, resulting in a form independent of the basis. This allows further theoretical development and numerical computations to be performed in the most suited basis for the task. Two terms must be converted

into matrix elements: the statistical weight and the oscillatory term. The former is expressed as the diagonal element of the density matrix,

$$\rho_i = \langle i | \rho | i \rangle , \quad (8)$$

where the operator

$$\rho = e^{-H/kT} / \text{Tr} (e^{-H/kT}) \quad (9)$$

is diagonal in the energy eigenstates basis. The second term can be written in terms of the time evolution operator  $U(t, 0)$ , which satisfies the Schrödinger equation

$$i\hbar \frac{dU}{dt} = HU \quad (10)$$

and the boundary condition  $U(0, 0) = I$ . Since  $H$  does not depend explicitly on time in Equation (1), the integration of Equation (10) yields the trivial solution  $U(t, 0) = e^{-iHt/\hbar}$ , which implies that

$$U|i\rangle = e^{-iE_i t/\hbar}|i\rangle , \quad U^\dagger|f\rangle = e^{iE_f t/\hbar}|f\rangle . \quad (11)$$

$C(t)$  can now be written as a trace over a product of quantum operators, a form that is independent of the representation of the states of the system

$$\begin{aligned} C(t) &= \sum_{if} e^{iE_f t/\hbar} \langle i | \mathbf{d} | f \rangle e^{-iE_i t/\hbar} \langle f | \mathbf{d}^\dagger | i \rangle \rho_i \\ &= \sum_{if} \langle i | \mathbf{d} U^\dagger | f \rangle \langle f | \mathbf{d}^\dagger U | i \rangle \rho_i \\ &= \text{Tr}(\mathbf{d}(U^\dagger \mathbf{d}^\dagger U) \rho) . \end{aligned} \quad (12)$$

## 2.2. Classical Path Approximation

The classical path method divides the system into two subsystems, the emitter and the perturbers, and treats them separately, making two approximations that disentangle the two sets of coordinates in Equation (12).

The weak coupling approximation assumes that the interaction potential  $V$  between the two subsystems is negligible relative to the kinetic energy of a perturber (Smith et al. 1969). The state of the perturbers remains independent of the state of the emitter despite the

interaction that produces line broadening (“no backreaction”). This has two consequences. First, the density matrix of the system becomes separable

$$\rho \propto e^{-(H_0+H_p+V)/kT} \approx e^{-H_0/kT} e^{-H_p/kT} \equiv \rho_a \rho_p , \quad (13)$$

where  $\rho_a$  and  $\rho_p$  only depend on the coordinates of the atom and the perturbers, respectively. Next, the wave function of the system can be approximated by the product of the perturbers and emitter wave functions, the latter being subject to a time-dependent interaction  $V(t)$ , with a Hamiltonian written as

$$H_a = H_0 + V(t) . \quad (14)$$

The autocorrelation function can now be written as two embedded traces over the perturbers and atomic coordinates

$$C(t) = \text{Tr}_p \{ \text{Tr}_a (\mathbf{d} U_a^\dagger \mathbf{d}^\dagger U_a) \rho_a \} , \quad (15)$$

where  $U_a$  is the time evolution operator of the emitter, which satisfies the equation

$$i\hbar \frac{dU_a}{dt} = H_a U_a . \quad (16)$$

The perturbers are still treated as quantum particles in Equation (15). The last step of the semi-classical approach is to approximate the wave function of the perturbers by a product of wave packets that are assumed to remain sufficiently localized during the characteristic timescale of the broadening process. This allows the replacement of  $V(t)$  by the corresponding classical potential function  $V(\mathbf{R}, \mathbf{x}(t))$ , where  $\mathbf{R}$  is the position operator of the radiating electron and  $\mathbf{x}$  is the set of classical 3D-coordinates of all perturbers.

The perturbers now follow classical trajectories with well-defined positions and velocities, and the trace over the states of the perturbers in Equation (15) is reinterpreted as an average over all possible configurations of perturbers, called the thermal average

$$C(t) = \{ \text{Tr}_a (\mathbf{d} U_a^\dagger \mathbf{d}^\dagger U_a \rho_a) \}_{\text{av}} , \quad (17)$$

where the weight of a configuration of perturbers of energy  $E_p$  is a Boltzmann factor proportional to  $e^{-E_p/kT}$ . In most He I line profile calculations, the interaction between perturbers is neglected, and the statistical weight is computed from their kinetic energies only, resulting



in a product of Maxwell velocity distributions. By separating the behavior of the classical perturbers from the state of the atom, a series of dynamic configurations of perturbers can then be defined, at least conceptually, prior to quantum mechanical calculations.

### 2.3. Calculation of the Autocorrelation Function

Equation (17) is still not applicable for practical calculations since it includes the contribution of all possible electronic transitions of the atom, and involves products of matrices of infinite dimension. The trace being independent of the choice of basis, we adopt the states of the isolated helium atom as the basis, and express the autocorrelation function as a product of 5 matrices:

$$C(t) = \left\{ \sum_{abb'a'a''} \langle a|\mathbf{d}|b\rangle \langle b|U^\dagger(t)|b'\rangle \langle b'|\mathbf{d}^\dagger|a'\rangle \langle a''|U(t,0)|a''\rangle \langle a''|\rho|a\rangle \right\}_{\text{av}}, \quad (18)$$

where every summation is formally performed over all unperturbed states of the atom, and  $U$  (with the  $a$  subscript omitted for clarity) now stands for the time evolution operator of the atom only. The dummy indices in the summation are limited to finite sets by the following arguments.

Every He I line in the optical and in the near UV range is the result of transitions between upper levels  $|n\ell m s\rangle$  with  $n \geq 3$  and lower levels  $|2\ell' m' s\rangle$  of the same spin  $s$ . For the calculation of a single line profile, the sets of  $|a\rangle$  and  $|b\rangle$  states are defined, respectively, as the upper and lower states of the transition under study. The states within each group share the same  $n$ ,  $\ell$ , and  $s$  quantum numbers, and differ only in their  $m$  values.

In this work, we neglect the perturbation of the lower levels, which are in general much less polarizable than the upper levels. This implies that  $\langle b|U^\dagger|b'\rangle = e^{iE_b t/\hbar} \delta_{bb'}$ , and the  $b'$  index can be removed from the summation in Equation (18). The density matrix  $\rho$  is further assumed to be diagonal in the unperturbed He I states basis, an approximation always used in practice in the calculations of He I profiles, to our knowledge. Moreover,  $\langle a|\rho|a\rangle$  has the same value for all  $|a\rangle$  states, which allows us to discard this multiplicative factor because the final profile will be normalized to unity. Combining these results, we find that

$$C(t) = \left\{ \sum_{aba'} e^{iE_b t/\hbar} \langle a|\mathbf{d}|b\rangle \langle b|\mathbf{d}^\dagger|a'\rangle \langle a'|U(t,0)|a\rangle \right\}_{\text{av}}. \quad (19)$$

As discussed in Appendix A, the upper states  $|a\rangle$ , when subjected to the potential  $V(t)$ , mix

with their neighboring states of the same spin, mainly those of the same quantum number  $n$ . In this work, the  $|a'\rangle$  states will be defined as the subspace of states with the same value of  $n$  for the upper states of the transition, a special case of the no-quenching approximation (Kolb & Griem 1958), which assumes that collisions do not cause transitions between states with different values of  $n$ . Thus, the  $|a\rangle$  states are a subset of the  $|a'\rangle$  set of states, which is disjoint from the lower  $|b\rangle$  states. For example, considering the  $2P^1 - 4D^1$   $\lambda 4922$  transition, the three sets of states are the seven states  $|4, \ell = 2, m, s = 0\rangle$  with  $|m| \leq 2$ , the 16 states  $|4\ell m, s = 0\rangle$  with  $\ell \leq 3$  and  $|m| \leq \ell$ , and the single state  $|2, \ell = 1, m, s = 0\rangle$  with  $|m| \leq 1$ .

Our last approximation is the definition of the potential  $V(t)$  in the definition of the time evolution operator of the atom in Equation (16). We only keep the first non-vanishing term in the multipole expansion of the interaction between the atom and the perturbers, which is the dipole term, which yields the Hamiltonian

$$H_a = H_0 + e\mathbf{F}(t) \cdot \mathbf{R} , \quad (20)$$

where  $\mathbf{F}$  is the electric field at the position of the emitter.

At this stage, the standard theory and the computer simulation approach take different routes for the integration of the Schrödinger equation of the time evolution operator of the atom (Equation 16), and for the calculations of the thermal average  $\{\dots\}_{\text{av}}$  over all configurations of classical perturbers.

### 3. Standard Stark Broadening Theory

This section presents a brief outline of the standard Stark broadening theory, and focuses on the core approximations of this theory, most of which are corrected by the computer simulation method.

#### 3.1. Basic Principles

The standard Stark broadening theory uses the quasi-static approximation for the ions and the impact approximation for the electrons. This section presents a summary of this theory for the simpler case where the lower levels of the transition are not significantly perturbed (see Baranger 1958b, 1962, Smith et al. 1969, Griem 1974, Barnard et al. 1969, and Sahal-Brechot 1969a,b, for a more general description of the theory).

Since the ions are assumed to be quasi-static, effects stemming from their motion are neglected, and the electric field associated with the presence of ions may be chosen to point arbitrarily toward the  $z$  direction. For each fixed configuration of ion perturbers, the Hamiltonian of the emitter immersed in the field  $F$  produced by the ions then becomes

$$H(t) = H_a + eFZ + V_e(t) \quad (21)$$

where  $V_e$  is the time-varying potential due to the electrons, and  $Z$  is the  $z$ -component of  $\mathbf{R}$ .

The interaction between ions and electrons is neglected, thus allowing the separation of the thermal average into averages over configurations of ions and electrons. Moreover, since the Hamiltonian (Equation 21) does not depend on the detailed configuration of the ions, except through the ion electric field, the average over the static ion configurations can be replaced by an average over ion electric fields, weighted by the microfield statistical distribution. The autocorrelation function of the profile then becomes

$$C(t) = \int_0^\infty dF W_R(F) \{C_e(t; F)\}_{\text{av}_e} \quad (22)$$

where  $C_e(t; F)$  is the autocorrelation function due to the moving electrons in the static field  $F$ . In this expression, the distribution of the microfield  $W_R(F)$  takes into account the correlation in the spatial distribution of the ions due to their mutual interactions, and is parameterized by  $R$ , the ratio of the mean distance between ions and the Debye radius (Hooper 1968).

The autocorrelation function  $C_e(t; F)$  for the electron is a generalization of Equation (19), now applied to the Hamiltonian in Equation (21)

$$C_e(t; F) = \sum_{\alpha b \alpha'} e^{iE_b t/\hbar} \langle \alpha | \mathbf{d} | b \rangle \langle b | \mathbf{d}^\dagger | \alpha' \rangle \{ \langle \alpha' | U_e(t; F) | \alpha \rangle \}_{\text{av}_e} , \quad (23)$$

where the summation is performed over all perturbed upper states  $|\alpha(F)\rangle$  of the helium atom subjected to the constant field  $F$ . Similarly, the time evolution operator satisfies the Schrödinger equation

$$i\hbar \frac{dU_e(t; F)}{dt} = (H_a + eFZ + V_e(t)) U_e(t; F) . \quad (24)$$

Finally, the “electronic” thermal average  $\{\dots\}_{\text{av}_e}$  is performed over all possible trajectories of the electrons.

### 3.2. The Impact Approximation

The electronic evolution operator  $U_e(t; F)$  that satisfies the Schrödinger equation (Equation 24) can be formally expanded as a Dyson series using perturbation theory,

$$U_e(t; F) = e^{-iH_a(F)t} \left[ 1 - \frac{i}{\hbar} \int_0^t dt_1 V'(t_1) + \left( -\frac{i}{\hbar} \right)^2 \int_0^t dt_1 \int_0^{t_1} dt_2 V'(t_1) V'(t_2) + \dots \right] \quad (25)$$

where the operator  $V'(t) \equiv e^{-iH_a(F)t} V_e(t; F) e^{iH_a(F)t}$ . The increasing complexity of the successive terms in the expansion makes the handling of overlapping collisions intractable, as well as the calculation of the contribution of a single collision.

The impact approximation avoids these problems by assuming that (1) strong collisions do not overlap in time, (2) the contribution of weak overlapping collisions can be approximated by the truncated expansion (Equation 25) up to second order, and (3) the collision time is much shorter than the inverse half width at half maximum of the line (the completed collision assumption). Performing the thermal average of the resulting  $U_e$  in Equation (23), and computing the inverse Fourier transform (Equation 7), then yield the line profile

$$I(\omega) = \int_0^\infty dF W_R(F) I_e(\omega; F) , \quad (26)$$

which is a weighted sum of electron-broadened profiles at constant ionic field

$$I_e(\omega; F) = -\frac{1}{\pi} \sum_{ab\alpha'} \langle \alpha | \mathbf{d} | b \rangle \langle b | \mathbf{d}^\dagger | \alpha' \rangle \langle \alpha' | [i(\omega - \omega_{\alpha b}) + \Phi]^{-1} | \alpha' \rangle , \quad (27)$$

where  $\hbar\omega_{\alpha b}$  is the energy difference between the perturbed upper states  $|\alpha\rangle$  and unperturbed lower states  $|b\rangle$ , and the collision operator  $\Phi$  represents the contribution of the electrons (in the impact regime) to broadening. Here, the dependence of the perturbed upper states, the perturbed energies, and the collision operator  $\Phi$  on the field  $F$  is omitted. The diagonalization process that yields the perturbed energies, as well as the unitary transformation between perturbed and unperturbed states, are discussed in Appendix A.

As a result of the impact approximation, the collision operator  $\Phi$  for a given electron number density  $N_e$  corresponds to the second order term of the expansion in Equation (25) integrated over the full trajectory of a single electron, and averaged over all possible trajectories

$$\Phi(F) = N_e \left( -\frac{i}{\hbar} \right)^2 \left\{ \int_{-\infty}^{\infty} dt_1 \int_{-\infty}^{t_1} dt_2 V'(t_1) V'(t_2) \right\}_{\text{av}_e} . \quad (28)$$

In this averaging process, the electron is assumed to move along a rectilinear trajectory at constant velocity, described by the expression

$$\mathbf{r}(t) = \boldsymbol{\rho} + \mathbf{v}(t - t_0) , \quad (29)$$

where  $\boldsymbol{\rho}$  and  $t_0$  are the position and time of nearest approach, respectively, and  $\mathbf{v}$  is the velocity perpendicular to  $\boldsymbol{\rho}$ . The impact parameter of the trajectory is the norm of  $\boldsymbol{\rho}$ .

The averaging process involves integrals over the impact parameter  $\rho \equiv |\boldsymbol{\rho}|$ , the orientation of the  $\boldsymbol{\rho}$  and  $\mathbf{v}$  vectors, as well as a weighted average over the Maxwell-Boltzmann velocity distribution. The integral over  $\rho$  is formally between 0 and infinity, but upper and lower cut-offs are defined for practical calculations. A maximal impact parameter  $\rho_{\text{max}}$ , of the order of the Debye radius, is used to approximate the screening effect due to the correlation in the spatial distribution of the electrons. A minimal impact parameter  $\rho_{\text{min}, \alpha\alpha'}(v; F)$  — a function of the velocity, different for each pair of states — is further required because the perturbation expansion (Equation 25) breaks down at small impact parameters, which produces a diverging integral. The collision operator  $\Phi$  is therefore computed as a sum of contributions from weak and strong collisions, characterized by impact parameters larger and smaller than  $\rho_{\text{min}}$ , respectively,

$$\Phi(F) = \Phi(F)^{\text{weak}} + \Phi(F)^{\text{strong}} . \quad (30)$$

The strong-collision term is calculated with a classical theory (Lorentz 1906), which is probably correct within a factor 2 (Griem et al. 1962).

In the far wings, the complete collision approximation of the impact theory is no longer valid. A unified theory that properly makes the transition from the impact to the quasi-static regime for the electron has been developed for hydrogen, taking advantage of the  $\ell$ -degeneracy of the levels (Vidal et al. 1970). There is however no such theory for the helium atom, and the impact broadening theory must therefore be replaced by the one-electron theory.

### 3.3. The One-Electron Theory

The one-electron theory of Baranger (1962) describes the profile in the line wings, where non-overlapping strong collisions contribute, and it also explains how the profile approximately turns into a quasi-static line profile. This theory is not applicable to the entire profile, however, and it even diverges in the line core. The one-electron theory is not formally considered as part of the standard Stark broadening theory, but it constitutes nevertheless the alternative in the far wing where the impact approximation is no longer valid. Fortunately, the interval of validity of the one-perturber approximation partially overlaps with that of the impact theory. The one-perturber theory describes the profile in the wings where  $\Delta\omega$  is much larger than the width of the line, while the impact theory is valid when  $\Delta\omega$  is less than a typical collision time.

In the one-perturber theory, Equation (27) remains valid, but the  $\Phi$  operator, as well as the minimal impact parameter  $\rho_{\min}$  that segregates weak and strong collisions, change with respect to the impact theory, and become frequency-dependent. There is no rigorous way to make the transition from one theory to the other. However, the profiles calculated separately from each theory are almost identical in their common overlapping region; the transition may thus be chosen quite arbitrarily. Such a method is described in Beauchamp et al. (1997).

### 3.4. Summary of Approximations

The standard Stark broadening theory thus includes several approximations, in addition to those already implied by the classical path approximation. Ion dynamics is neglected, overlapping electronic collisions are treated approximately, and the contribution from weak and strong electronic collisions are modelled in distinct ways.

Another issue — linked to the profile normalization process — occurs when one combines the standard theory with the one-electron theory. As shown by Kolb & Griem (1958), the standard theory yields, by construction, a profile with a well-defined area equal to

$$\int I(\omega)d\omega = \sum_{ab} |\langle a|\mathbf{d}|b\rangle|^2 . \quad (31)$$

It is then trivial to normalize the profile to unit area as required for synthetic spectrum calculations. When combining the impact theory for the line core with the one-electron theory in the wings, this normalization process is no longer valid, which constitutes a formal

weakness of this approach.

The purpose of the computer simulation approach is to lift these approximations, while retaining the important aspects of the semi-classical approach.

## 4. Computer Simulations

### 4.1. Overview of the Approach

The purpose of the computer simulation approach is to integrate the Schrödinger equation (Equation 16) for the time evolution operator  $U(t, 0)$  of the perturbed emitter, without resorting to the truncated power series approximation of the analytical theory. This method considers correctly the effect of overlapping collisions on line broadening, regardless of their duration, thus unifying the treatment of ions and electrons. The numerical integration process treats indifferently weak and strong electronic collisions, whose types were defined only in the context of the semi-analytical theory. Moreover, the transition between the two electron broadening regimes — namely, the impact regime in the core and the one-electron regime in the wings —, as well as ion dynamics, are managed naturally by this method.

The semi-classical approximation remains in force: the perturbers move along classical paths, corresponding to straight lines when their mutual interaction is neglected, and when the emitter is neutral. The classical potential  $V(t)$  is still approximated by the first terms in the dipole expansion of the electrostatic potential. In this work, we keep the first non-vanishing term that led to the Hamiltonian given in Equation (20). We apply the  $\mu$ -ion model from Seidel & Stamm (1982), where a stationary emitter is located at the center of a fixed simulation volume. In this model, it is the motion of the perturbers in the rest frame of the emitter that is being simulated.

The thermal average of the autocorrelation function (Equation 19), which corresponds to an average over the set of all possible configurations of dynamic perturbers, is approximated by an average over a large, but finite set of configurations, whose statistical properties are representative of the infinite set. The autocorrelation function is then written as an average over  $N$  autocorrelation functions  $C_i(t)$ , each one calculated for a given configuration  $i$ ,

$$C(t) = \frac{1}{N} \sum_{i=1}^N C_i(t) . \quad (32)$$

The line profile then follows from the numerical Fourier transform (Equation 7). The whole process guarantees that the profile can be properly normalized, thus resolving the issue raised in Section 3.4.

Each dynamic configuration consists of a spherical simulation volume of finite radius  $R$ , a single emitter located at the center of the sphere, and a set of charged perturbers moving along classical paths and generating a time-varying electric field  $\mathbf{F}(t)$  at the position of the emitter. The radius must ensure that the expected statistical distribution of the electric field intensity is recovered. As discussed by Hegerfeldt & Kesting (1988), this radius must be of the order of the Debye radius.

The value of  $C_i$  — the autocorrelation function of the  $i$ th scenario — is calculated for a series of discrete times  $t_k = k\Delta$ , in two separate steps. First, a time sequence of electric field  $\mathbf{F}_i(t_k)$  at the origin of the simulation volume is generated from the spatial distribution of moving perturbers at that time. Equation (16) is then integrated in order to get the time evolution operator  $U_i(t_k)$ . The validity of the simulation method thus rests on the procedure for generating the dynamic configurations, and for calculating the time evolution operator.

## 4.2. Properties of the Simulation Volume

### 4.2.1. The Perturber-Emitter Interaction

In these computer simulations, perturbers follow straight line trajectories, and the effect of the spatial correlation produced by their mutual interaction is thus neglected. As discussed in Section 3.1, this correlation has a measurable impact on the statistical distribution  $W(F)$  of the microfield. A more realistic simulation should take into account the effect on their trajectory of the Coulomb interaction between the perturbers. The resulting distribution of the microfields would then be in agreement with the Hooper distribution, but at the cost of a prohibitive computing time.

The microfield distribution resulting from computer simulations with rectilinear trajectories corresponds to the Holtsmark distribution, a special case of the  $W(F)$  distribution for independent particles. In such calculations, the perturber-emitter interaction is described by a Coulomb field. A way to recover the proper microfield distributions with rectilinear trajectories is to replace the physically valid Coulomb potential with a Debye potential (Gigosos et al. 2003; Stambulchik et al. 2007). The microfield distribution is then well reproduced, including in the far wings where the contribution from individual strong collisions become important. In what follows, we adopt a Debye potential to describe the required perturber-emitter interaction.



#### 4.2.2. *The Simulation Volume and the Impact Coordinate System*

The simulation volume consists of three concentric spheres, all centered on the position of the emitter. The smallest sphere corresponds to the exclusion volume, with a radius of the order of the Bohr radius. The particles never cross this volume in order to avoid both penetrating and high-energy collisions, for which case the classical path approximation breaks down. The second sphere, called the calculation volume, includes the perturbers that contribute to the electric field at the position of the emitter. In our simulations, its radius is set to three times the Debye radius computed by considering all perturbers (electrons and ions). Hegerfeldt & Kesting (1988) demonstrated that the resulting microfield distribution reproduces adequately the theoretical distribution  $W(F)$  from Hooper (1968), discussed in Section 4.2.1, if the perturber-emitter interaction is described by a Debye potential. The third and largest sphere, called the simulation volume, is limited by a radius equal to three times the Debye radius of the electrons (excluding ions). Among the perturbers in the simulation volume, only those present in the calculation volume contribute to the electric field, allowing the possibility of simulating the variation of the local number density in the calculation volume. This important aspect was first introduced by Hegerfeldt & Kesting (1988). The number of particles in the calculation volume then follows a Poisson distribution.

The coordinate system that gives the best control over the trajectory generation process is the impact coordinate system, described by Hegerfeldt & Kesting (1988). These coordinates are :

1. the impact parameter  $b$ , which is the distance of closest approach between the emitter and the perturber,
2. the velocity  $v$  of the perturber,
3. the time  $t_0$  of closest approach,
4. the angle  $\alpha$  that defines the trajectory of the perturber in the plane formed by the point of closest approach  $\mathbf{b}$  and the velocity vector,
5. the angles  $\phi$  and  $\theta$  that define the orientation of the velocity vector.

In this coordinate system, the position of the perturber is

$$\mathbf{r}(t) = b(\hat{v}_1 \cos \alpha + \hat{v}_2 \sin \alpha) + \hat{v}_3 v(t - t_0), \quad (33)$$

where the vectors  $\hat{v}_1$ ,  $\hat{v}_2$ , and  $\hat{v}_3$  form an orthonormal basis,

$$\begin{aligned}\hat{v}_1 &= (-\cos\phi\cos\theta, -\sin\phi\cos\theta, \sin\theta) \\ \hat{v}_2 &= (-\sin\phi, \cos\phi, 0) \\ \hat{v}_3 &= (\cos\phi\sin\theta, \sin\phi\sin\theta, \cos\theta).\end{aligned}\tag{34}$$

In Equation (33),  $\mathbf{r}$  is perpendicular to  $\hat{v}_3$  when  $t = t_0$ , as required.

The advantages of this coordinate system are two-fold. First, an appropriate choice of the coordinate  $t_0$  constrains each perturber to be inside the simulation volume at the initialization phase of the simulation ( $t = 0$ ), once the velocity  $v$  and the impact parameter  $b$  have been assigned. Second, a proper value of the impact parameter further guarantees that the impact vector is within the simulation volume, but outside the exclusion volume, in the vicinity of the emitter.

### 4.3. Generation and Rejection of Particles

One of the most challenging difficulties with computer simulations is to maintain a consistent number of perturbers, in a fixed simulation volume, which satisfies the joint distribution of space and velocity, without introducing undesirable correlations. To deal with this problem, Gigoso & Cardenoso (1996) proposed a simulation approach that combines an initialization phase and a particle reinjection process. Particles are first placed inside the simulation volume at  $t = 0$ . As the simulation evolves, some particles leave the volume and are replaced by new particles of the same type, which enter the volume and follow a straight line trajectory inside the sphere. The outgoing particles are excluded for the rest of the simulation.

The particle generation process is a crucial step in the simulation. It must ensure that in a given simulation volume, the statistical properties of the system are maintained at all times, and at every single time considering all simulations running in parallel. To do so, the coordinates of each perturber must be generated randomly from their joint statistical distribution. Luckily, this distribution can be written as a product of distributions of the six phase space coordinates. A uniform random number generator can then be used to generate a random number, which is then mapped onto the desired value based on the statistical distribution of the generated coordinates. Two mapping strategies are applied below: the inverse transformation method (Press et al. 2007), and a method based on cells (Gigoso & Cardenoso 1996).

The statistical distribution of each coordinate is obtained with the following reasoning. The probability that a perturber is found inside an infinitesimal volume  $d^3\mathbf{r} d^3\mathbf{v}$  of the phase

space is proportional to the product of this volume (in order to satisfy the constraint of an isotropic and homogeneous space) with a Boltzmann weight  $e^{-v^2/v_T^2}$ . Using the Jacobian  $|\partial(\mathbf{r}, \mathbf{v})/\partial(\alpha, t_0, b, \phi, \theta, v)|$ , the joint probability distribution in the impact coordinate system becomes

$$f(\alpha, t_0, b, \phi, \theta, v) \propto bv^3 e^{-v^2/v_T^2} \sin \theta . \quad (35)$$

However, since the simulation volume has a finite radius, the perturbers must also respect at  $t = 0$  the following condition

$$|\mathbf{r}|^2 = b^2 + v^2 t_0^2 \leq R^2 , \quad (36)$$

which translates into a constraint on the  $t_0$  coordinate

$$|t_0| \leq t_{0,\max} , \quad (37)$$

where  $t_{0,\max}$  is a function of both the velocity  $v$  and the impact parameter  $b$

$$t_{0,\max} \equiv \frac{\sqrt{R^2 - b^2}}{v} . \quad (38)$$

Hence, the variables  $b$ ,  $v$ , and  $t_0$  are not statistically independent even if the distribution (Equation 35) is separable. This statistical dependency is taken into account when the initial coordinates of the particles are randomly generated.

The joint distribution of the three variables, written as

$$f(t_0, b, v) \propto bv^3 e^{-v^2/v_T^2} , \quad (39)$$

can be expressed as the following product of conditional distributions

$$f(t_0, b, v) = f_t(t_0|b, v) f_b(b|v) f_v(v) , \quad (40)$$

where the  $|$  symbol stands for “given”. Therefore, the 3-variable  $f$  distribution becomes the product of the distribution of  $t_0$  (given  $b$  and  $v$ ),  $b$  (given  $v$ ), and  $v$ . Since  $t_0$  is uniform between the  $\pm t_{0,\max}$  limits (for given  $b$  and  $v$ ), we can write

$$f_t(t_0|b, v) = \frac{1}{2t_{0,\max}} = \frac{v}{2\sqrt{R^2 - b^2}} . \quad (41)$$

By substituting this result into Equation (39), we find that

$$f_b(b|v) \propto b\sqrt{R^2 - b^2} , \quad (42)$$

an expression independent of  $v$ . This, in turn, implies that  $b$  and  $v$  can be generated independently. Finally, the two previous results can be combined to yield the Maxwell-Boltzmann distribution for the velocity

$$f_v(v) \propto v^2 e^{-v^2/v_T^2} . \quad (43)$$

The initialization process respects the joint statistical distribution of the coordinates at time  $t = 0$ . The values of the coordinates  $\alpha$ ,  $\phi$ , and  $t_0$  are found by applying a linear transformation on the output of the uniform number generator over the interval  $(0,1)$ , given that their statistical distribution is uniform. The generation of the variable  $\theta$  (with  $f(\theta) \propto \sin \theta$ ) is obtained with the inverse transformation method.

The generation of the  $b$  and  $v$  coordinates follows a method developed by Gigoso & Cardeñoso (1996) based on cells. The main advantage of this method is to prevent a progressive displacement of the particles towards the surface of the sphere, an apparent cooling of the plasma, as well as an undesired correlation between the two coordinates. The statistical distribution of  $b$  is first divided into  $N_p$  cells of equal probability (where  $N_p$  is the number of particles of type  $p$ ). Each particle is then assigned to a cell, and its  $b$  value is chosen randomly from within the interval associated with the cell. The method is similar for  $v$ , but the statistical distribution is divided into  $N_p + 1$  cells instead. Each particle is assigned to a  $v$ -cell, leaving one empty cell. This empty cell plays a crucial role in the reinjection process.

A particle reinjection process ensures that the joint statistical distribution of coordinates remains unchanged (within normal fluctuations) over the entire length of the simulation. When a particle leaves the volume, a new particle of the same type is randomly positioned at the surface of the simulation volume. Its coordinates are then computed as follows. The new particle is assigned to the same  $b$ -cell as the leaving particle, and the impact parameter is generated randomly from within this cell. For the velocity, the particle is assigned to the empty cell, and the cell of the leaving particle becomes the empty cell. The value of the  $t_0$  coordinate is fixed, given  $b$  and  $v$ , by the constraint that the particle is at the surface of the outer sphere. Finally, the angular coordinates ( $\alpha$ ,  $\theta$ , and  $\phi$ ) are generated with the same method as in the initialization phase.

#### 4.4. The Time Evolution Operator

Once an electric field sequence has been generated over a succession of  $N$  consecutive times  $t_k \equiv k\Delta t$  (with  $k = 0$  to  $N - 1$ ), the time evolution operator  $U(t_k, 0)$  of the perturbed atom must be calculated. The numerical integration of Equation (10) is performed using

the solution for a Hamiltonian  $H$  with no explicit time dependence,  $U(t_1, t_0) = e^{-iH(t_1-t_0)/\hbar}$ , as well as two properties of the time evolution operator: (1) the time continuity condition,  $U(t, t) = I$ , and (2) the composition property,  $U(t_2, t_0) = U(t_2, t_1)U(t_1, t_0)$ . These last two properties allow us to write  $U(t_k, 0)$  as a product of operators, computed over all previous time intervals

$$U(t_k, 0) = \prod_{j=0}^{k-1} U(t_{j+1}, t_j) . \quad (44)$$

This last equation is exact for any set of increasing values of  $t_j$ , but is not applicable unless  $U(t_{j+1}, t_j)$  can effectively be calculated.

Following Gigosos & Cardenoso (1996), we make the approximation that the electric field, and hence the Hamiltonian operator  $H$ , remain constant in every time interval  $(t_j, t_{j+1})$ . These are denoted by  $\mathbf{F}_j$  and  $H_j$ , respectively. The following Schrödinger equation

$$i\hbar \frac{dU(t, t_{j-1})}{dt} = [H_0 + e\mathbf{F}_{j-1} \cdot \mathbf{R}] U(t, t_{j-1}) \quad (45)$$

is then solved, one evolution operator at a time,

$$U(t_j, t_{j-1}) = e^{-iH_{j-1}\Delta t/\hbar} , \quad (46)$$

which leads to

$$U(t_k, 0) = \prod_{j=1}^k e^{-iH_{j-1}\Delta t/\hbar} = e^{-iH_{k-1}\Delta t/\hbar} U(t_{k-1}, 0) . \quad (47)$$

This numerical integration scheme guarantees that the time evolution operator is unitary.

The matrix elements of the time evolution operator are defined in the base  $|a\rangle$  of the unperturbed states of the helium atom in Equation (19). It is however much simpler to first diagonalize  $U(t_k, t_{k-1})$  in the base of the perturbed states  $|\alpha\rangle$ , specific to this time interval, and then to carry out the unitary transformation that transforms  $U$  into the base of the unperturbed states. As discussed in the Appendix A, the diagonalization of the operator  $H$  with a constant electric field yields the energies  $E_\alpha$  of the perturbed states, and the transformation matrix with coefficients  $\langle a|\alpha\rangle$ . This process is repeated at every time step for the operator  $H_{k-1}$ . The matrix elements of  $U$  in the unperturbed basis then become

$$\begin{aligned} \langle a|U(t_k, 0)|a'\rangle &= \sum_{\alpha\alpha'a''} \langle a|\alpha\rangle \langle \alpha|e^{-iH_{k-1}\Delta t/\hbar}|\alpha'\rangle \langle \alpha'|a''\rangle \langle a''|U(t_{k-1}, 0)|a'\rangle \\ &= \sum_{\alpha\alpha''} \langle a|\alpha\rangle e^{-iE_\alpha\Delta t/\hbar} \langle \alpha|a''\rangle \langle a''|U(t_{k-1}, 0)|a'\rangle , \end{aligned} \quad (48)$$

where the subscript  $k-1$  is omitted for the perturbed energies  $E_\alpha$ , and perturbed states  $|\alpha\rangle$  and  $|\alpha'\rangle$ .

This integration procedure assumes that the variation of the electric field is negligible during the time step  $\Delta t$ . The latter must thus be chosen carefully to insure that this approximation remains valid, while keeping computing time to a minimum. A characteristic time for the temporal variation of the electric field is the collision time of the fastest perturbers, i.e. the electrons. We use the time step proposed by Gigoso & Cardenoso (1996), which is one hundredth of the electron collision time

$$\Delta t = 0.01 \frac{r_0}{v_T} = 0.01 \left( \frac{3}{4\pi N_e} \right)^{1/3} \left( \frac{2kT}{\mu_e} \right)^{-1/2}, \quad (49)$$

where  $r_0$  is the typical distance between plasma charges whose electron number density is  $N_e$ ,  $v_T$  is the thermal velocity of the electrons,  $k$  is the Boltzmann constant, and  $T$  is the plasma temperature. The thermal velocity is computed with the reduced mass  $\mu_e$ , consistent with the  $\mu$ -ion model.

Most spectral lines presented in this work were computed by averaging the autocorrelation function over 25,000 simulation volumes, each one producing a time sequence of 50,000 electric field vectors  $\mathbf{F}(t_k)$ . The energy levels  $E_\alpha$  and states  $|\alpha\rangle$  of the perturbed helium atom were calculated at each time step  $t_k$ , in order to update the time evolution operator and the autocorrelation function  $C(t_k)$ . This calculation was parallelized on a cluster of computers. The typical computing time for a line at a given electronic density and temperature varied from 4095 to 32,760 CPU hours.

## 5. Results

We produced detailed profiles for six neutral helium lines, only two of which have previously published profiles obtained with the computer simulation approach, to our knowledge. The corresponding transitions show a wide range of behaviors, which allow us to test our own computer simulations under various physical conditions. Note that our line profiles are not convolved with a Doppler profile, to allow a direct comparison with those of Gigoso & González (2009) and Lara et al. (2012). We also compare our results with a new series of line profiles similar to those described by Beauchamp et al. (1997), based on the standard Stark broadening theory. These profiles have been calculated explicitly for this work, using the same approximations as in our computer simulations and neglecting the correction for the occupation probability formalism introduced by Hummer & Mihalas (1988). More specifically (1) the contribution of the lower levels to the broadening is neglected, (2) the perturbed upper levels are restricted to those with the same quantum number  $n$  as the upper level of the permitted transition, (3) the dipole matrix elements are calculated with the method of Oertel & Shomo (1968), and (4) the integral over the ionic field (Equation 22) extends to

infinity; it is not truncated to the critical value at which the highest Stark levels with a given  $n$  merge with other levels (Hummer & Mihalas 1988; Seaton 1990; Beauchamp et al. 1997). In addition, the two sets of profiles were generated for the same grid of temperatures, electron densities, and frequency, allowing for a more direct comparison. Since ions are assumed to be quasi-static in the standard Stark broadening theory, differences between both sets of calculations are expected particularly in the line cores, where ion dynamics — neglected in the standard theory — is properly managed by the computer simulation approach (Gigosos & González 2009).

In what follows, we present our profile calculations for the following helium lines: He I  $\lambda 4471$   $2P^3 - 4D^3$ ,  $\lambda 4922$   $2P^1 - 4D^1$ ,  $\lambda 5877$   $2P^3 - 3D^3$ ,  $\lambda 6678$   $2P^1 - 3D^1$ ,  $\lambda 4026$   $2P^3 - 5D^3$ , and  $\lambda 4144$   $2P^1 - 6D^1$ . The He I  $\lambda\lambda 4471$  and  $4922$  lines are the strongest in DB white dwarf spectra, and they represent special cases for which different implementations of the Stark broadening theory have been compared over the last fifty years or so (Griem 1968; Barnard et al. 1969; Calisti et al. 1988; Schoning 1994; Beauchamp et al. 1997; Gigosos & González 2009; Lara et al. 2012). Our grid covers electron number densities from  $N_e = 1 \times 10^{14}$   $\text{cm}^{-3}$  to  $6 \times 10^{17}$   $\text{cm}^{-3}$ , and temperatures of  $T = 10,000$  K,  $20,000$  K, and  $40,000$  K, which are relevant for synthetic spectrum calculations. We are interested here in lower densities in order to reproduce the physical conditions encountered in the upper atmospheric layers of white dwarfs where the line cores are formed. We also present exploratory calculations at  $N_e = 10^{16}$   $\text{cm}^{-3}$  and  $T = 20,000$  K for four additional helium lines: He I  $\lambda\lambda 5877$  and  $6678$ , whose upper level has the principal quantum number  $n = 3$ , as well as He I  $\lambda\lambda 4026$  and  $4144$ , with  $n$  higher than 4.

## 5.1. Helium Transitions with Upper Level $n = 4$

### 5.1.1. He I $\lambda 4471$

Profiles for the He I  $\lambda 4471$  line are displayed in Figures 1 to 3 for various values of temperature and electron density. The profiles for  $N_e = 10^{15}$   $\text{cm}^{-3}$ , shown in Figure 1, correspond to the lowest density available in the calculations of Gigosos & González (2009). Any difference between our computer simulations and theirs will require some explanation, because we followed essentially the same approach.

As expected, the main difference between our profiles, obtained from computer simulations, and those of Beauchamp et al. (1997), based on the standard Stark broadening theory, is for the low-density regime, near the line core of the permitted and forbidden components, as well as between them. This difference, of the order of a factor of 2 for some profiles, is due

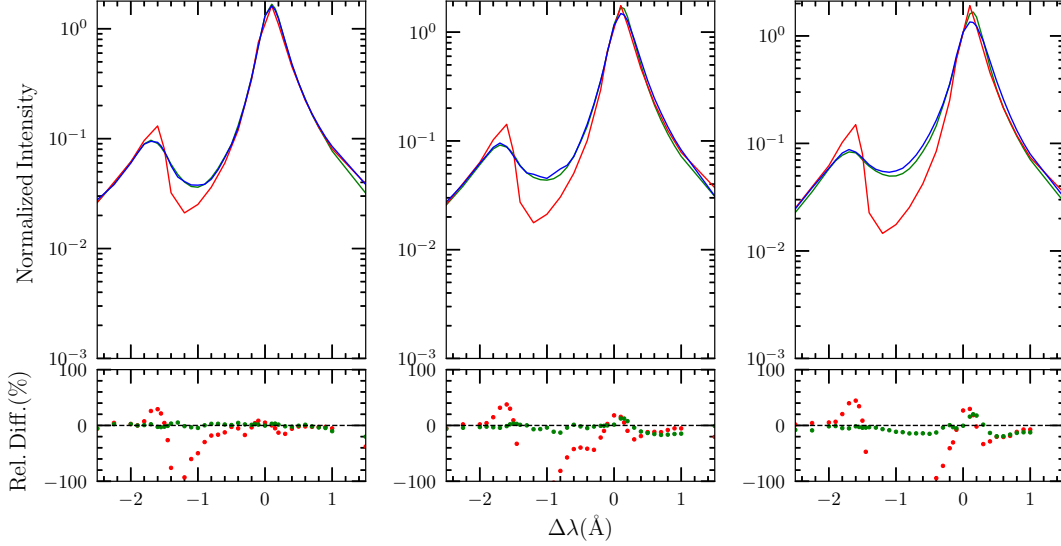


Fig. 1.— He I  $\lambda 4471$  line profiles obtained from our computer simulations (blue line) compared with those of Beauchamp et al. (1997, red line) and Gigosos & González (2009, green line). The profiles are shown for  $N_e = 10^{15} \text{ cm}^{-3}$  and for temperatures of  $T = 10,000 \text{ K}$ ,  $20,000 \text{ K}$ , and  $40,000 \text{ K}$ , from left to right. For a better comparison, the relative differences (in %) are displayed below each panel with the same colors as those used in the upper panel.

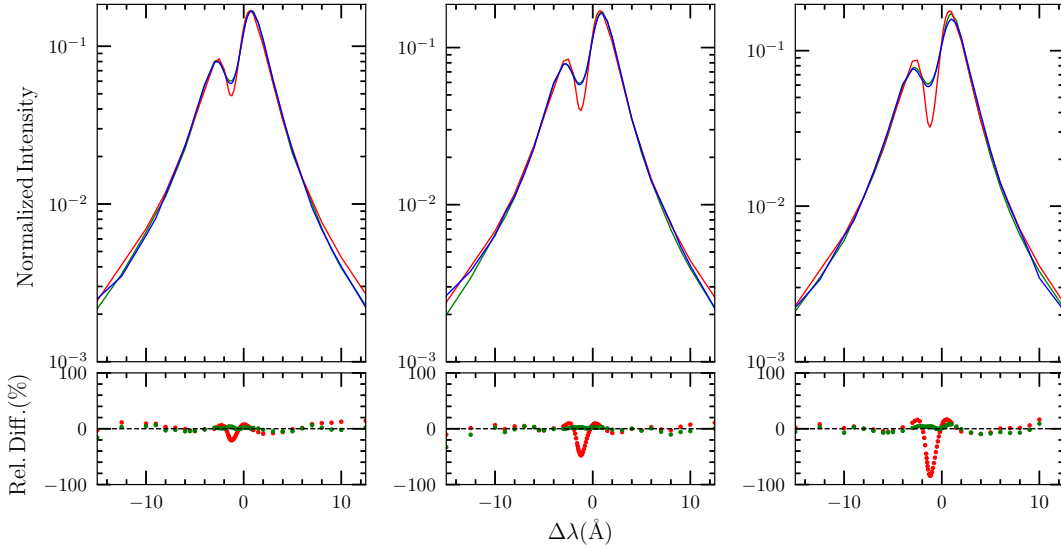


Fig. 2.— Same as Figure 1 but with  $N_e = 10^{16} \text{ cm}^{-3}$ .



to ion dynamics, whose effect is known to be important at low densities (Barnard et al. 1974; Gigosos & Cardenoso 1996; Gigosos & González 2009; Ferri et al. 2014). Both sets of profiles become almost identical at high densities, however, when ion dynamics becomes negligible. We conclude that the main difference between the two sets of profiles is in the treatment of ion dynamics, and that the other approximation made in the work of Beauchamp et al. (1997), namely the treatment of the transition between the impact and the one-electron regimes, seems appropriate at high densities, at least for this particular line.

Another reason must be invoked to account for the differences between our profiles and those of Gigosos & González (2009), given that our simulation environment is strongly inspired by their work. In this case, the main difference between our approach and theirs lies in the design of the simulation volume. As described in Section 4.2.2, our model consists of a calculation volume, defined as the volume that includes the perturbers contributing to the electric field at the position of the emitter, as well as a larger simulation volume. The particle reinjection process involves the simulation volume, which allows for local density variations, as properly implemented in the computer simulations of Hegerfeldt & Kesting (1988). In the work of Gigosos & Gonzalez, these two spheres are identical, and the number of perturbers therefore remains constant in the calculation volume. No study has shown that one approach is better than the other. For comparison purposes, we generated a new grid of profiles with identical calculation and simulation volumes, the results of which are displayed in Figure 4. Our profiles and those of Gigosos & Gonzalez now overlap almost perfectly. The comparison between the results shown in Figures 1 and 4 reveals that the impact of local density variations is important mostly in the region between the permitted and the forbidden components ( $\Delta\lambda \sim -1 \text{ \AA}$ ), as well as in the core of the permitted component. The minor differences that remain at higher temperature in the core of the latter component (see rightmost panel of Figure 4) still require an explanation.

In general, the three grids of profiles for He I  $\lambda 4471$  are in excellent agreement at high densities, where ion dynamics is less important, thus demonstrating the validity of the semi-analytical approach in this regime.

### 5.1.2. He I $\lambda 4922$

The profiles for He I  $\lambda 4922$  are presented in Figures 5 to 7 for the same temperatures and electron densities as before. The differences between our profiles obtained from computer simulations and those calculated using the standard Stark broadening can be explained again in terms of the effect of ion dynamics, similar to that already discussed in the context of the He I  $\lambda 4471$  line, in particular at low densities, near the line cores, and in the region between

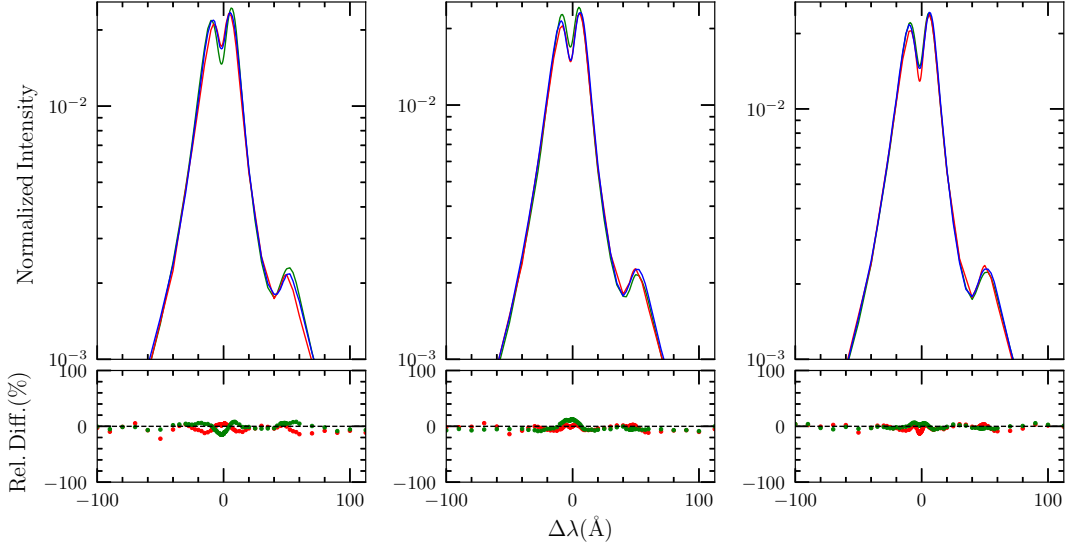


Fig. 3.— Same as Figure 1 but with  $N_e = 10^{17} \text{ cm}^{-3}$ .

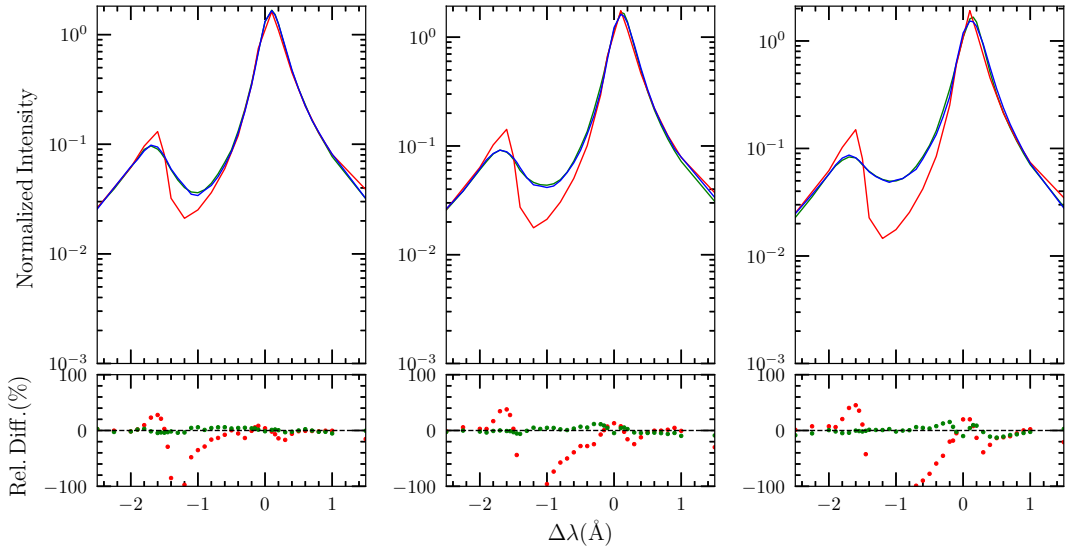


Fig. 4.— Same as Figure 1, but without taking into account local density variations, as properly implemented in the simulations of Hegerfeldt & Kesting (1988). Our profiles (blue line) then resemble more those of Gigosos & González (2009, green line), where this effect was neglected.

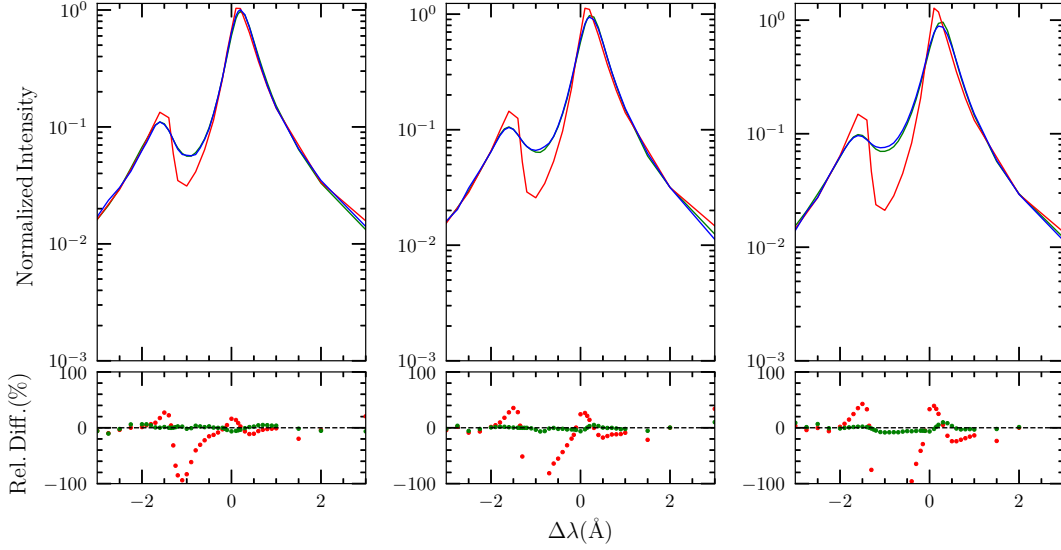


Fig. 5.— He I  $\lambda 4922$  line profiles obtained from our computer simulations (blue line) compared with those of Beauchamp et al. (1997, red line) and Lara et al. (2012, green line). The profiles are shown for  $N_e = 10^{15} \text{ cm}^{-3}$  and for temperatures of  $T = 10,000 \text{ K}$ ,  $20,000 \text{ K}$ , and  $40,000 \text{ K}$ , from left to right. For a better comparison, the relative differences (in %) are displayed below each panel with the same colors as those used in the upper panel.

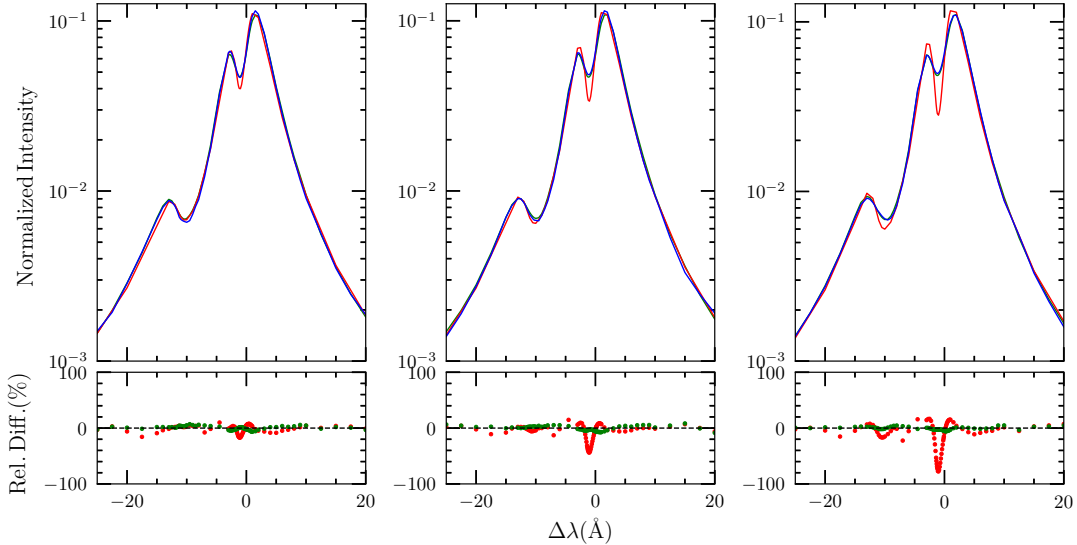


Fig. 6.— Same as Figure 5 but with  $N_e = 10^{16} \text{ cm}^{-3}$ .

the permitted component and its nearest forbidden component. The effect of ion dynamics can also be observed near the forbidden component at  $\Delta\lambda \sim -10 \text{ \AA}$  in Figure 6. The differences between our He I  $\lambda 4922$  profiles and the computer simulations from Lara et al. (2012, see Figure 5), based on the same approach as Gigoso & González (2009), are smaller than the differences observed previously for He I  $\lambda 4471$ , especially at  $T = 40,000 \text{ K}$ , although they do occur in the same range of wavelength. As before, it is possible to demonstrate that these differences are due to our treatment of local density variations, by generating a new grid of profiles where such variations are neglected. The results of this experiment, displayed in Figure 8, confirm this interpretation. Hence, the origin of these differences, as well as those for He I  $\lambda\lambda 4471$  and  $4922$ , is the inclusion of local density variations in our computer simulations.

The results presented so far for He I  $\lambda\lambda 4471$  and  $4922$  confirm that our computer simulation environment reproduces the published profiles adequately, including those obtained from independent simulations that take into account the contribution of lower levels perturbation and interference to broadening. This also demonstrates that the contribution of the lower states and interference between the lower and higher states, neglected in our simulations, are dominated by that of the upper states for these two transitions. We expect that the relative contribution of the lower states term will be more important for transitions from  $n = 2$  to  $n = 3$  (He I  $\lambda\lambda 5877$  and  $6678$ ). This will be investigated further in a future paper. Furthermore, we also validated the versatility of our implementation by easily adapting our calculations to different energy levels. We can now explore new He I transitions, characterized by upper levels with a principal quantum number different than  $n = 4$ , for which the only published detailed profiles have been obtained from the standard Stark broadening theory.

## 5.2. Helium Transitions with Upper Level $n = 3$

We compare in Figures 9 and 10 the profiles for the He I  $\lambda 5877 \ 2P^3 - 3D^3$  and  $\lambda 6678 \ 2P^1 - 3D^1$  lines, respectively, obtained from our computer simulations with those calculated using the standard Stark broadening theory (Beauchamp et al. 1997). The comparisons displayed here differ significantly from those shown above for He I  $\lambda\lambda 4471$  and  $4922$ . Neutral helium transitions involving an upper state with a principal quantum number  $n = 3$  are generally isolated lines at the electron densities considered in this work, and they are characterized by a Lorentzian shape, with a weak and distant forbidden component, resulting from the high energy differences between the upper level of the permitted transition and its neighboring levels. The closest forbidden component for He I  $\lambda 5877$  is  $\lambda 6068 \ 2P^3 - 3P^3$ .

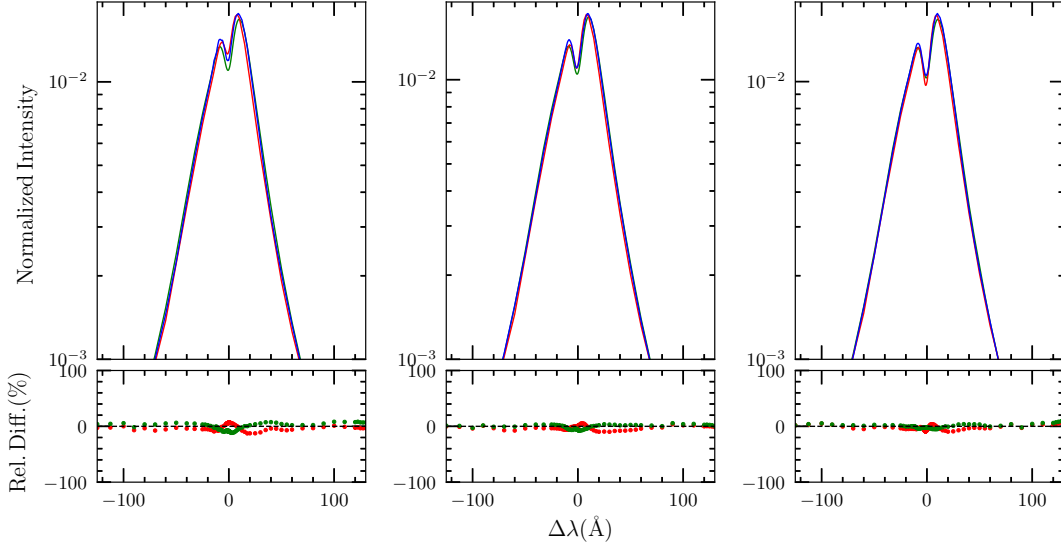


Fig. 7.— Same as Figure 5 but with  $N_e = 10^{17} \text{ cm}^{-3}$ .

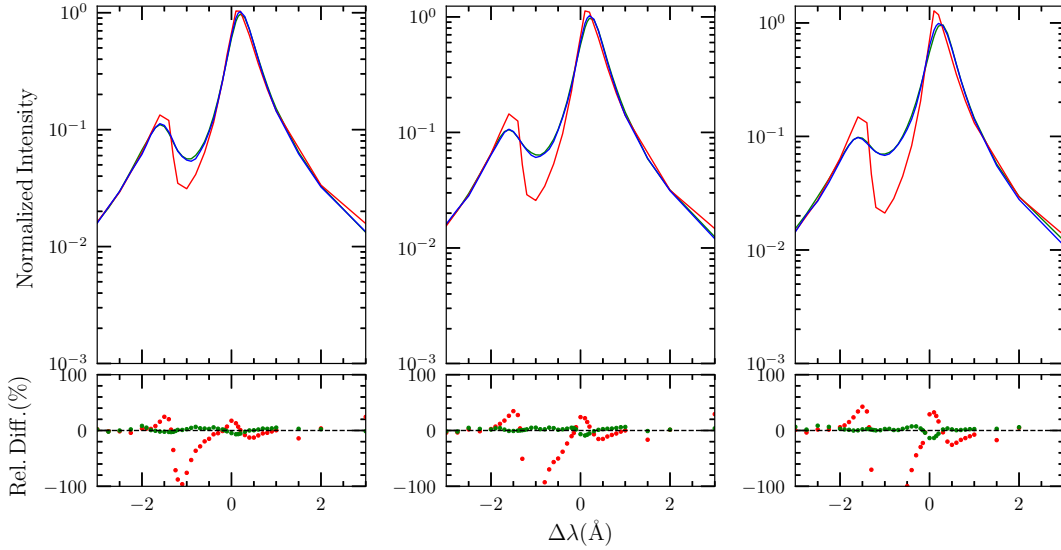


Fig. 8.— Same as Figure 5, but without taking into account local density variations, as properly implemented in the simulations of Hegerfeldt & Kesting (1988). The differences between our profiles (blue line) and those of Lara et al. (2012, green line) are of the same order as those observed in Figure 4.

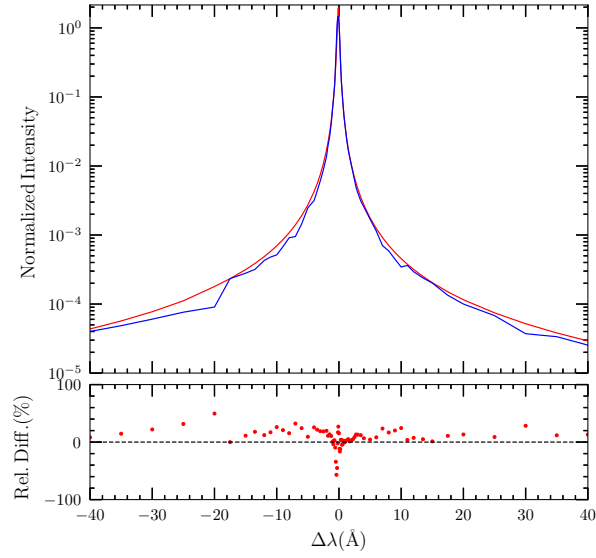


Fig. 9.— He I  $\lambda 5877$  line profile obtained from our computer simulations (blue line) compared with that of Beauchamp et al. (1997, red line), for  $N_e = 10^{16} \text{ cm}^{-3}$  and  $T = 20,000 \text{ K}$ . The relative differences (in %) are displayed at the bottom with the same colors as those used in the upper panel.

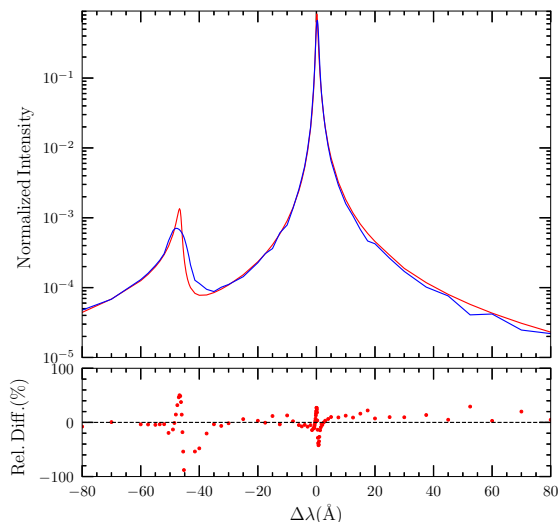


Fig. 10.— He I  $\lambda 6678$  line profile obtained from our computer simulations (blue line) compared with that of Beauchamp et al. (1997, red line), for  $N_e = 10^{16} \text{ cm}^{-3}$  and  $T = 20,000 \text{ K}$ . The relative differences (in %) are displayed at the bottom with the same colors as those used in the upper panel.

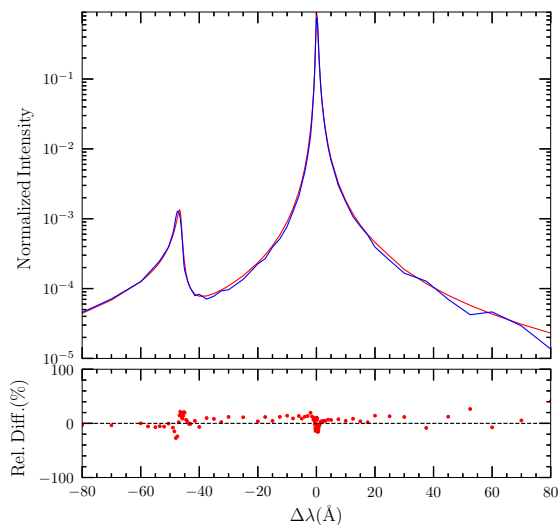


Fig. 11.— Same as Figure 10 but without taking ion dynamics into account in the computer simulation. The largest difference with the results displayed in Figure 10 occurs for the forbidden component.

This forbidden component constitutes a challenge for the simulation method, because its extremely low intensity, especially in the wings, could easily be misrepresented as a result of numerical noise. The profile for He I  $\lambda 6678$  includes the very asymmetrical forbidden component  $\lambda 6632 2P^1 - 3P^1$ . Despite its apparent simplicity, a Lorentzian-like line profile represents another challenge for computer simulations. Indeed, since the permitted component of these two lines is very narrow, and that the forbidden component is at much lower intensities, it is necessary to improve the wavelength (or frequency) resolution and to decrease the numerical noise. This implies increasing both the number of time steps and simulation volumes. A larger number of simulated volumes yields a better representation of the microfield distribution for the stronger, less likely, electric fields that contribute in the wings of the profile. For He I  $\lambda 5877$ , a simulation time of 70,000 time steps and 50,000 simulation volumes were required to define properly the permitted component and to reduce the numerical noise, respectively. Some residual noise remains in the wings of the profile displayed in Figure 9, despite these modifications. For He I  $\lambda 6678$ , 60,000 time steps and 60,000 simulation volumes were required to properly define the permitted and forbidden components.

The He I  $\lambda 6678$  line profile represents an interesting case. Although the shape of its permitted component is very similar between both sets of calculations displayed in Figure 10, there are important differences in the shape of the forbidden component. The most plausible explanation for the more rounded shape of the forbidden component obtained with our computer simulations is the additional broadening produced by ion dynamics. To test this hypothesis, we generated a profile with a version of our computer simulation in which the ions are at rest. The results, displayed in Figure 11, indicate that indeed, the forbidden component calculated with quasi-static ions now closely resemble that predicted by the standard Stark broadening theory (despite the presence of numerical noise). The effect of ion dynamics therefore remains important for this forbidden component, even at densities as high as  $N_e = 10^{16} \text{ cm}^{-3}$ .

So far, we have shown that our computer simulation framework reproduces well the profiles of some isolated lines, as well as lines with forbidden components that are well-separated from the permitted component. We now consider the case of helium lines involving upper levels for which  $n > 4$ , which are almost hydrogenic.

### 5.3. Helium Transitions with Upper Level $n > 4$

Similar comparisons for the He I  $\lambda 4026 2P^3 - 5D^3$  and  $\lambda 4144 2P^1 - 6D^1$  lines are displayed in Figures 12 and 13, respectively. For these lines, the permitted component is



superimposed on the strong forbidden components  $2P - nP, F, G$  because these upper levels, of almost identical energy in the isolated helium atom, are mixed by the electric field. The width of the lines tends to increase with the principal quantum number  $n$  for a given electron density and temperature. This behavior can be appreciated by comparing the results shown in Figures 12 and 13 — which both correspond to transitions with an upper level  $n = 5$  and  $n = 6$ , respectively — with the results displayed in Figures 9 and 10 for  $n = 3$ .

The calculation of these profiles is numerically demanding since the dimension of the matrices for which the eigenvalues and eigenvectors have to be extracted increases as  $n^2$ . However, the absence of narrow structures in the profiles implies that a lower resolution in wavelength (or frequency) is sufficient to represent the profile correctly. The profile for He I  $\lambda 4144$  ( $n = 6$ ) was computed with 40,000 time steps, instead of the 50,000 time steps required for the He I  $\lambda 4026$  ( $n = 5$ ) profile. The latter also shows the forbidden component  $\lambda 4045$   $2P^3 - 5P^3$ , as well as a complex behavior near the peak of the profile, where the permitted component mixes with other forbidden components. The profiles of these two lines calculated with our computer simulations compare well with those produced with the standard Stark broadening theory, at this electron density. Ion dynamics appears to have less impact on these line profiles than for He I  $\lambda\lambda 4471$  and  $4922$  at an electron density of  $N_e = 10^{16} \text{ cm}^{-3}$ .

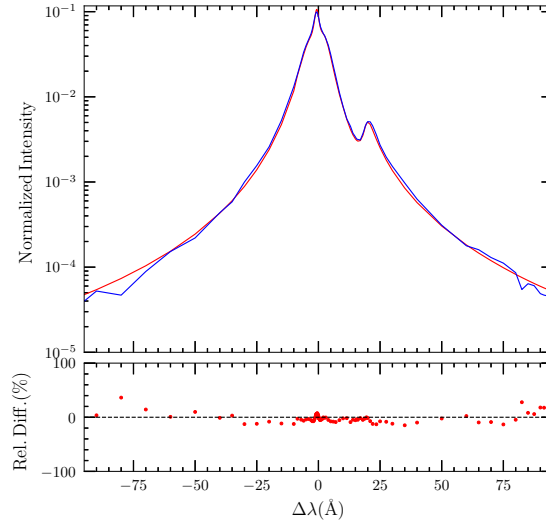


Fig. 12.— Same as Figures 9 and 10 but for the He I  $\lambda 4026$  line.

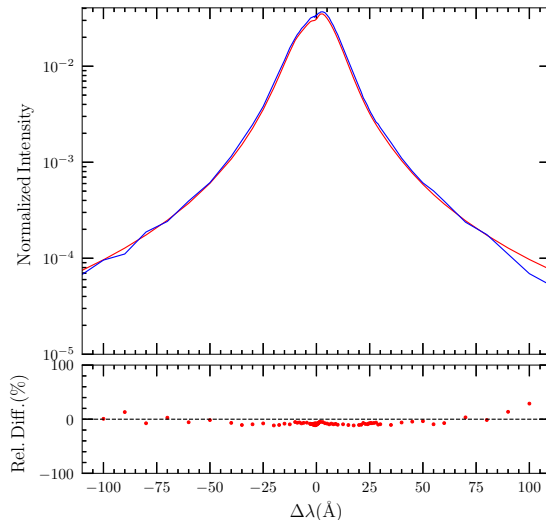


Fig. 13.— Same as Figures 9 and 10 but for the He I  $\lambda 4144$  line.

#### 5.4. Application to White Dwarf Model Spectra

As discussed in the Introduction, the atmospheric parameters of white dwarf stars can be measured using the so-called spectroscopic technique, where absorption line profiles are compared with the predictions of detailed model atmospheres. Given the limited number of He I profiles calculated in this paper, it is too early at this stage to present a full-fledged spectroscopic analysis of DB (helium-line) white dwarfs. However, it is still possible to perform a few quantitative comparisons with preexisting material.

The calculations of model atmospheres require to solve simultaneously the radiative transfer equation, the hydrostatic equilibrium equation, and the radiative equilibrium equation, which is replaced by a flux conservation equation in the presence of convective energy transport. It is customary under most white dwarf conditions to assume local thermodynamic equilibrium (LTE), which allows the use of the standard Saha-Boltzmann equations to describe the ionization and excitation equilibrium. The solution of these equations provides the temperature and pressure structure as a function of optical depth. In a second step, the detailed emergent monochromatic flux — referred to as the synthetic spectrum — can be calculated by solving the radiative transfer equation using the previously calculated thermodynamic structure. The most important physical quantity in these calculations is the extinction (or opacity) coefficient,  $\chi_\nu$ , which describes all absorption (bound-bound, bound-free, free-free) and diffusion (Thomson and Rayleigh scattering) processes. Thus in principle,

the line absorption profiles (bound-bound opacity) may affect the emergent flux, but also the overall atmospheric structure. Since we have only a limited number of improved He I profiles at our disposal, we will compare, in what follows, the results of synthetic spectra using two different sets of line profile calculations, but by keeping the thermodynamic structures fixed.

Our model atmospheres are similar to those employed by Bergeron et al. (2011). These are built from the model atmosphere code described at length in Tremblay & Bergeron (2009) and references therein, which incorporate the Stark profiles of neutral helium of Beauchamp et al. (1997). As discussed above, these detailed profiles for over 20 lines of neutral helium take into account the transition from quadratic to linear Stark broadening, the transition from the impact to the quasistatic regime for electrons, as well as forbidden components. The input parameters of model atmospheres are the effective temperature ( $T_{\text{eff}}$ ), the surface gravity ( $\log g$ ), and the chemical composition, which we assume here to be pure helium (H/He=0).

The comparison of synthetic spectra calculated using the profiles of Beauchamp et al. (1997) with those obtained from our computer simulations differ from the comparisons already discussed in the previous subsections. Indeed, a stellar line profile is not representative of unique temperature and electron density, but instead is formed at different depths in the stellar atmosphere. For instance, the line core, where the opacity is the largest, is formed high in the atmosphere where both the temperature and density are low. In contrast, the line wings, where the opacity is significantly reduced, are formed in the deeper photospheric regions, where the temperature and density are much larger, and more characteristic of the regions where the continuum is formed.

Since we possess a complete grid of improved profiles only for He I  $\lambda\lambda 4471$  and  $4922$ , we restrict our comparison of synthetic spectra for these two lines. In Figure 14, we compare the (normalized) Eddington fluxes ( $H_\nu$ ) at  $T_{\text{eff}} = 13,000$  K,  $18,000$  K, and  $30,000$  K at  $\log g = 8.0$ , which span the range of temperatures for DB white dwarfs. Also shown are synthetic spectra for the two hottest models at  $\log g = 7.0$  where the differences are more significant. These comparisons reveal that our improved Stark profiles yield results that are remarkably similar to those obtained with our earlier calculations at all temperatures where DB white dwarfs are found, at least for these two lines. The results indicate that our computer simulations are able to produce Stark profiles that are perfectly suited in the context of DB white dwarfs, and also that the more approximate calculations of Beauchamp et al. (1997) seem appropriate in the physical regime explored here. This overall agreement is not unexpected given that the temperature and electron density regime corresponds to the range of parameters where our new Stark profiles and those of Beauchamp et al. (1997) agree the best (see Section 5).

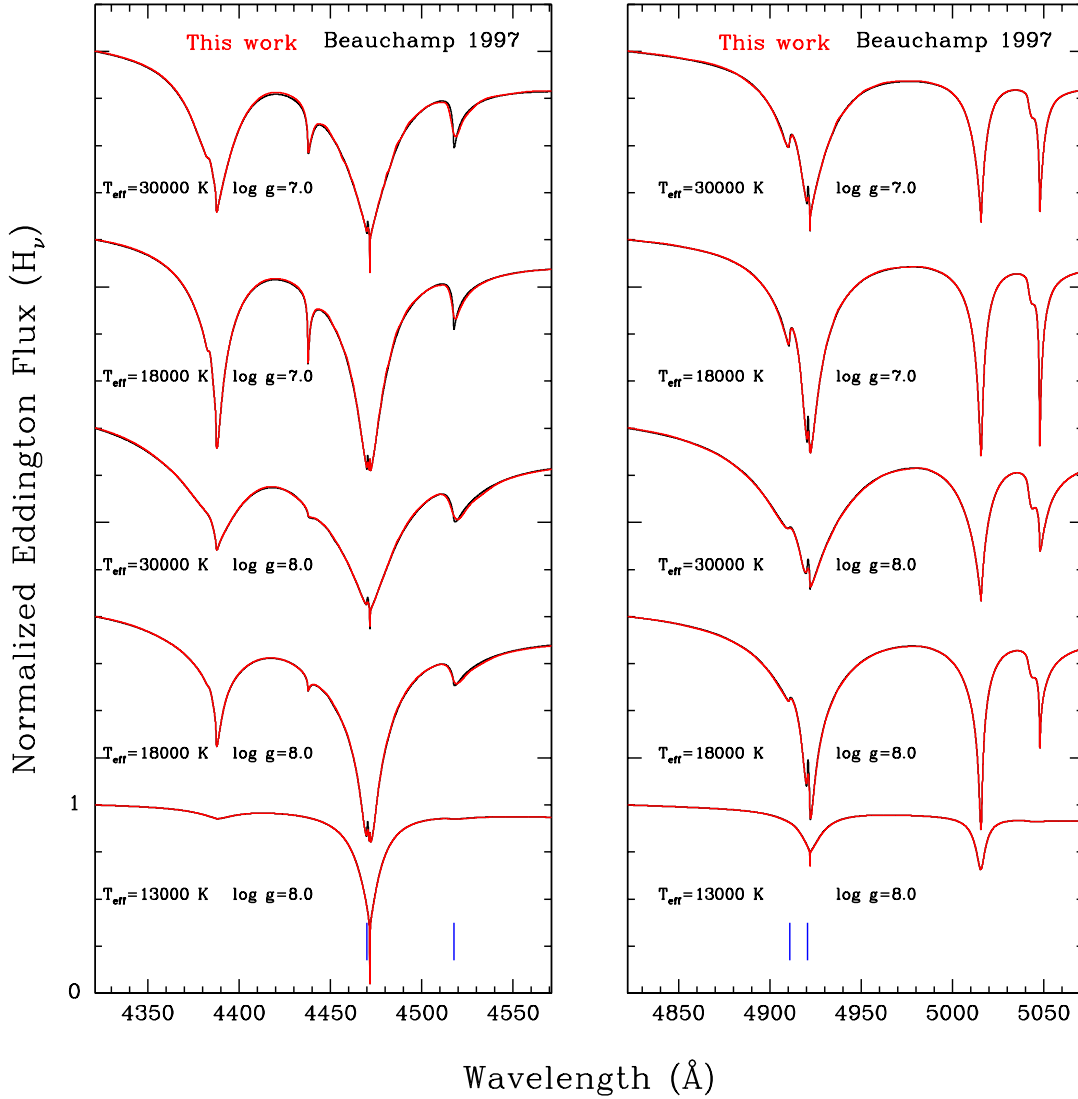


Fig. 14.— Comparison of synthetic spectra for DB white dwarfs near He I  $\lambda 4471$  (left) and He I  $\lambda 4922$  (right) produced with our new Stark broadened profiles (red lines) and the profiles of Beauchamp et al. (1997, black lines). All spectra are normalized to a continuum set to unity and offset from each other for clarity. The effective temperature and surface gravity are indicated in the panels; a pure helium composition is assumed throughout. The location of all forbidden components are indicated by blue tick marks at the bottom.

There are still subtle differences, however, between both sets of calculations near the farthest forbidden component of He I  $\lambda 4471$ , as well as near the line core; these differences are also more significant at lower surface gravities. This is a direct consequence of the inclusion of ion dynamics into our simulations (see also Figure 10 as well as Barnard et al. 1974, 1975; Gigosos & González 2009; Lara et al. 2012), while these ions are assumed to be quasi-static in the earlier calculations of Beauchamp et al. (1997). For the region near He I  $\lambda 4922$ , the forbidden components are closer to the line core but similar differences can be observed. Obviously, these effects will require extremely high resolution and high signal-to-noise spectroscopic observations to be measured.

Given that we have complete grids of computer simulation profiles for only two lines, it is too early to assess the implications of our results on the temperature and mass scales of DB white dwarfs. In particular, we need to produce detailed Stark profiles for the He I  $\lambda 3820$  and  $\lambda 4388$  lines, which are particularly log  $g$ -sensitive in the context of DB white dwarfs. Such results will be reported in due time. Also, our computer simulations can find applications in other astrophysical contexts as well, such as the UV-bright star Barnard 29, recently analyzed by Dixon et al. (2019), who showed that ion dynamics — using the profiles of Barnard et al. (1975) — provided a better match to the He I  $\lambda 4922$  line (see their Figure 8) over Stark profiles where these effects were neglected.

## 6. Conclusion

We presented new calculations of Stark broadened profiles for the He I  $\lambda\lambda 4471$  and  $4922$  lines using computer simulations performed by combining the method developed by Gigosos & Cardeñoso (1996) for treating the dynamics of the environment around the emitting neutral helium atom, and the approach of Hegerfeldt & Kesting (1988) for dealing with local density variations. These line profiles offer a better representation of the ion dynamics than the semi-analytical calculations of Beauchamp et al. (1997), and they also represent a different view of the computer simulations discussed by Gigosos & González (2009) and Lara et al. (2012), who did not consider the effect of local density variations. By also neglecting this effect in our calculations, we were able to properly test the validity of our computer simulation environment, by reproducing almost perfectly the He I  $\lambda\lambda 4471$  and  $4922$  profiles published by Gigosos & González (2009) and Lara et al. (2012), respectively.

An exploration of narrower helium lines, such as He I  $\lambda\lambda 5877$  and  $6678$ , showed that the shape of the permitted components is Lorentzian-like, while their forbidden components behave much differently. In particular, we were able to demonstrate — by removing the effect of ion dynamics from our computer simulations and by comparing the results with those of

Beauchamp et al. (1997) — that the forbidden component of He I  $\lambda 6678$  is significantly affected by this effect. Also, an exploration of broader lines, such as He I  $\lambda\lambda 4026$  and  $4144$ , showed how the CPU time required in our simulations increases dramatically for transitions to higher principal numbers  $n$ , as a result of the larger amount of neighboring energy levels to be included in the calculations. Fortunately, since there are no narrow features in these profiles, some of the computing time can be reduced by decreasing the simulation time.

Although we were able to produce profiles for a total of six neutral helium lines so far, the computer simulation approach begins to show its limitation regarding the amount of effort required to optimize the quality of the line profile calculations, given the amount of memory space and CPU time required to perform the simulation. Thus, additional numerical challenges remain to be dealt with before we are able to produce full grids of He I line profiles. Nevertheless, the results obtained so far from our computer simulations represent a most encouraging and promising avenue of investigation.

Despite the improvements for the He I  $\lambda\lambda 4471$  and  $4922$  line profiles obtained from our computer simulations, their implementation into the calculations of synthetic spectra of DB white dwarfs did not show any appreciable difference with respect to the previous calculations of Beauchamp et al. (1997). This is mostly because the physical conditions where these lines are formed correspond to the range where both sets of calculations agree the best. As such, our improved calculations can be viewed as an important validation of the approximations made by Beauchamp, at least for these two lines. A more detailed comparison with other He I lines will be presented in future work.

Finally, our computer simulations should eventually provide a new environment for exploring other physical problems encountered in the modeling of white dwarf atmospheres, such as the Stark broadening of hydrogen lines in DA stars, and perhaps even van der Waals broadening in DB stars. In future work, we also expect to lift some of the approximations discussed in this paper (see Section 2), namely the neglect of the mixing of lower levels, the mixing of upper levels with levels of different  $n$ , and the quadrupolar term in the multipole expansion of the potential, as carried out by Gomez et al. (2016) for hydrogen.

### Acknowledgments

This work is supported in part by the NSERC Canada and by the Fund FRQ-NT (Quebec).

### A. Appendix: The Perturbed He I State Basis

Integration of the time evolution operator (Equation 46) and computation of the electron-broadened profile (Equation 27) for a field  $F$  — whether within the impact or the one-electron approximation — use the perturbed basis  $|\alpha(F)\rangle$ , and not the set of energy states  $|a\rangle$  of the isolated helium atom. Since the dipole matrix elements are only known in the unperturbed basis, a unitary transformation must be found to perform the change of basis. The unitary transformation and the energy of the perturbed states are found by solving an eigenvalue problem. Here, we consider this problem for a field  $\mathbf{F}$  of arbitrary orientation. The special case of a field along the  $z$  direction applies to the quasi-static field from ions in the standard theory.

The perturbed states are a solution to the following Schrödinger equation

$$H_a(\mathbf{F})|\alpha\rangle = E_\alpha|\alpha\rangle , \quad (\text{A1})$$

where  $|\alpha\rangle$  corresponds to the normalized quantum state, with energy  $E_\alpha$ , of the perturbed helium. The perturbed states are projected into the subspace of  $|a\rangle$  unperturbed upper states

$$|\alpha\rangle = \sum_a \langle a|\alpha\rangle |a\rangle , \quad (\text{A2})$$

where  $\langle a|\alpha\rangle$  are the transformation coefficients from the unperturbed to the perturbed basis, which is normalized such that  $\langle\alpha|\alpha\rangle = 1$ .

By combining Equations (A1) and (A2), and by multiplying the resulting equation by the unperturbed state set  $\langle a'|$ , we obtain the following eigenvalue problem

$$\sum_{a'} (\Omega_{aa'} - E_\alpha \delta_{aa'}) \langle a'|\alpha\rangle = 0 , \quad (\text{A3})$$

where

$$\Omega_{aa'} = \mathbf{F} \cdot \langle a|\mathbf{d}|a'\rangle + E_a \delta_{aa'} \quad (\text{A4})$$

is Hermitian, with real eigenvalues  $E_\alpha$ . The eigenvectors  $\langle a|\alpha\rangle$  are then normalized so that  $\langle\alpha|\alpha\rangle = 1$ . Most elements of  $\Omega$  vanish, a consequence of the properties of the Clebsch-Gordan coefficients, which also lead to selection rules for electric dipole transitions.

## REFERENCES

- Alexiou, S., Glenzer, S., & Lee, R. W. 1999a, *Phys. Rev. E*, 60, 6238
- Alexiou, S., Sauvan, P., Poqu eruse, A., Leboucher-Dalimier, E., & Lee, R. W. 1999b, *Phys. Rev. E*, 59, 3499
- Baranger, M. 1958a, *Physical Review*, 112, 855
- . 1958b, *Physical Review*, 111, 481
- . 1962, *Pure and Applied Physics*, 13, 493
- Barnard, A. J. & Cooper, J. 1970, *J. Quant. Spec. Radiat. Transf.*, 10, 695
- Barnard, A. J., Cooper, J., & Shamey, L. J. 1969, *A&A*, 1, 28
- Barnard, A. J., Cooper, J., & Smith, E. W. 1974, *J. Quant. Spec. Radiat. Transf.*, 14, 1025
- . 1975, *J. Quant. Spec. Radiat. Transf.*, 15, 429
- Beauchamp, A. 1995, PhD thesis, Universit  de Montral
- Beauchamp, A., Wesemael, F., & Bergeron, P. 1997, *ApJS*, 108, 559
- Beauchamp, A., Wesemael, F., Bergeron, P., Liebert, J., & Saffer, R. A. *Astronomical Society of the Pacific Conference Series*, Vol. 96, *The DB and DBA white dwarfs: epitomes of hydrogen-deficient stars*, ed. C. S. Jeffery & U. Heber, 295
- Ben Chaouacha, H., Sahal-Br chot, S., & Ben Nessib, N. 2007, *A&A*, 465, 651
- Bergeron, P., Dufour, P., Fontaine, G., Coutu, S., Blouin, S., Genest-Beaulieu, C., B dard, A., & Rolland, B. 2019, *ApJ*, 876, 67
- Bergeron, P., Leggett, S. K., & Ruiz, M. T. 2001, *ApJS*, 133, 413
- Bergeron, P., Ruiz, M. T., & Leggett, S. K. 1997, *ApJS*, 108, 339
- Bergeron, P., Saffer, R. A., & Liebert, J. 1992, *ApJ*, 394, 228
- Bergeron, P., Wesemael, F., Dufour, P., Beauchamp, A., Hunter, C., Saffer, R. A., Gianninas, A., Ruiz, M. T., Limoges, M. M., Dufour, P., Fontaine, G., & Liebert, J. 2011, *ApJ*, 737, 28
- Calisti, A., Stamm, R., & Talin, B. 1988, *Phys. Rev. A*, 38, 4883



- Dimitrijevic, M. S. & Sahal-Brechot, S. 1984, *J. Quant. Spec. Radiat. Transf.*, 31, 301
- Dixon, W. V., Chayer, P., Reid, I. N., & Miller Bertolami, M. M. 2019, *AJ*, 157, 147
- Eisenstein, D. J., Liebert, J., Koester, D., Kleinmann, S. J., Nitta, A., Smith, P. S., Barentine, J. C., Brewington, H. J., Brinkmann, J., Harvanek, M., Krzesiński, J., Neilsen, Eric H., J., Long, D., Schneider, D. P., & Snedden, S. A. 2006, *AJ*, 132, 676
- Ferri, S., Calisti, A., Mossé, C., Rosato, J., Talin, B., Alexiou, S., Gigosos, M., González, M., González-Herrero, D., Lara, N., Gomez, T., Iglesias, C., Lorenzen, S., Mancini, R., & Stambulchik, E. 2014, *Atoms*, 2, 299
- Frerichs, M. R. 1989, *Zeitschrift fur Physik D Atoms Molecules Clusters*, 11, 315
- Gaia Collaboration, Babusiaux, C., van Leeuwen, F., Barstow, M. A., Jordi, C., Vallenari, A., Bossini, D., Bressan, A., Cantat-Gaudin, T., van Leeuwen, M., & et al. 2018, *A&A*, 616, A10
- Genest-Beaulieu, C. & Bergeron, P. 2019a, *ApJ*, 871, 169
- . 2019b, *ApJ*, 882, 106
- Gieske, H. A. & Griem, H. R. 1969, *ApJ*, 157, 963
- Gigosos, M. A. 2014, *Journal of Physics D Applied Physics*, 47, 343001
- Gigosos, M. A. & Cardenoso, V. 1996, *Journal of Physics B Atomic Molecular Physics*, 29, 4795
- Gigosos, M. A. & Cardenoso, V. 1987, *Journal of Physics B Atomic Molecular Physics*, 20, 6005
- Gigosos, M. A., Fraile, J., & Torres, F. 1985, *Phys. Rev. A*, 31, 3509
- Gigosos, M. A. & González, M. Á. 2009, *A&A*, 503, 293
- Gigosos, M. A., González, M. Á., & Cardenoso, V. 2003, *Spectrochimica Acta*, 58, 1489
- Gigosos, M. A., González-Herrero, D., Lara, N., Florido, R., Calisti, A., Ferri, S., & Talin, B. 2018, *Phys. Rev. E*, 98, 033307
- Gomez, T. A. 2017, PhD thesis, University of Texas
- Gomez, T. A., Nagayama, T., Kilcrease, D. P., Montgomery, M. H., & Winget, D. E. 2016, *Phys. Rev. A*, 94, 022501

- Griem, H. R. 1968, *ApJ*, 154, 1111
- Griem, H. R. 1974, *Spectral line broadening by plasmas* (New York: Academic Press)
- Griem, H. R., Baranger, M., Kolb, A. C., & Oertel, G. 1962, *Physical Review*, 125, 177
- Halenka, J. & Olchawa, W. 1996, *J. Quant. Spec. Radiat. Transf.*, 56, 17
- Halenka, J., Olchawa, W., Grabowski, B., & Gajda, F. 2002, *J. Quant. Spec. Radiat. Transf.*, 74, 539
- Hegerfeldt, G. C. & Kesting, V. 1988, *Phys. Rev. A*, 37, 1488
- Hooper, C. F. 1968, *Physical Review*, 169, 193
- Hummer, D. G. & Mihalas, D. 1988, *ApJ*, 331, 794
- Kepler, S. O., Kleinman, S. J., Nitta, A., Koester, D., Castanheira, B. G., Giovannini, O., Costa, A. F. M., & Althaus, L. 2007, *MNRAS*, 375, 1315
- Kepler, S. O., Pelisoli, I., Koester, D., Reindl, N., Geier, S., Romero, A. D., Ourique, G., Oliveira, C. d. P., & Amaral, L. A. 2019, *MNRAS*, 486, 2169
- Koester, D. & Kepler, S. O. 2015, *A&A*, 583, A86
- Kolb, A. C. & Griem, H. 1958, *Physical Review*, 111, 514
- Lara, N., González, M. Á., & Gigos, M. A. 2012, *A&A*, 542, A75
- Lorentz, H. A. 1906, *Koninklijke Nederlandse Akademie van Wetenschappen Proceedings Series B Physical Sciences*, 8, 591
- Oertel, G. K. & Shomo, L. P. 1968, *ApJS*, 16, 175
- Olchawa, W. 2002, *J. Quant. Spec. Radiat. Transf.*, 74, 417
- Olchawa, W., Olchawa, R., & Grabowski, B. 2004, *European Physical Journal D*, 28, 119
- Omar, B., Günter, S., Wierling, A., & Röpke, G. 2006, *Phys. Rev. E*, 73, 056405
- Poquérousse, A., Alexiou, S., & Klodzh, E. 1996, *J. Quant. Spec. Radiat. Transf.*, 56, 153
- Press, W., Teukolsky, S., Vetterling, W., & Flannery, B. 2007, *Numerical Recipes: the art of scientific computing* (Cambridge: Cambridge University Press)
- Sahal-Brechot, S. 1969a, *A&A*, 1, 91

- . 1969b, *A&A*, 2, 322
- Schoning, T. 1994, *Journal of Physics B Atomic Molecular Physics*, 27, 4501
- Seaton, M. J. 1990, *Journal of Physics B Atomic Molecular Physics*, 23, 3255
- Seidel, J. & Stamm, R. 1982, *Journal of Quantitative Spectroscopy and Radiative Transfer*, 27, 499
- Shamey, L. J. 1969, PhD thesis, University of Colorado at Boulder.
- Smith, E., Vidal, C., & Cooper, J. 1969, *Journal of Research of the National Bureau of Standards*, 73A
- Smith, E. W., Cooper, J., & Vidal, C. R. 1969, *Physical Review*, 185, 140
- Sorge, S. & Günter, S. 2000, *European Physical Journal D*, 12, 369
- Stambulchik, E., Fisher, D. V., Maron, Y., Griem, H. R., & Alexiou, S. 2007, *High Energy Density Physics*, 3, 272
- Stambulchik, E. & Maron, Y. 2006, *J. Quant. Spec. Radiat. Transf.*, 99, 730
- Stamm, R. & Voslamber, D. 1979, *J. Quant. Spec. Radiat. Transf.*, 22, 599
- Tonry, J. L., Stubbs, C. W., Lykke, K. R., Doherty, P., Shivvers, I. S., Burgett, W. S., Chambers, K. C., Hodapp, K. W., Kaiser, N., Kudritzki, R.-P., Magnier, E. A., Morgan, J. S., Price, P. A., & Wainscoat, R. J. 2012, *ApJ*, 750, 99
- Tremblay, P. E. & Bergeron, P. 2009, *ApJ*, 696, 1755
- Tremblay, P. E., Bergeron, P., & Gianninas, A. 2011, *ApJ*, 730, 128
- Vidal, C. R., Cooper, J., & Smith, E. W. 1970, *J. Quant. Spec. Radiat. Transf.*, 10, 1011
- Voss, B., Koester, D., Napiwotzki, R., Christlieb, N., & Reimers, D. 2007, *A&A*, 470, 1079
- Wujec, T., Jazgara, A., Halenka, J., & Musielok, J. 2003, *The European Physical Journal D - Atomic, Molecular, Optical and Plasma Physics*, 23, 405
- Wujec, T., Olchawa, W., Halenka, J., & Musielok, J. 2002, *Phys. Rev. E*, 66, 066403
- Ya’akobi, B., George, E. V., Bekefi, G., & Hawryluk, R. J. 1972, *Journal of Physics B Atomic Molecular Physics*, 5, 1017